A Model for the Graphite Formation in Ductile Cast Iron: Part I. Inoculation Mechanisms

T. SKALAND, Ø. GRONG, and T. GRONG

Part I of this investigation deals with the inoculation mechanisms in ductile cast iron, with particular emphasis on the theoretical aspects of heterogeneous nucleation of graphite at inclusions. It is shown that the majority of the inclusions in ductile cast iron are primary or secondary products of the magnesium treatment (*e.g.*, MgS, CaS, $MgO \cdot SiO_2$, and $2MgO \cdot SiO_2$). After inoculation with (X,Al)-containing ferrosilicon (X denotes Ca, Sr, or Ba), hexagonal silicate phases of the $XO \cdot SiO_2$ or the $XO \cdot Al_2O_3 \cdot 2SiO_2$ type form at the surface of the oxide inclusions, probably through an exchange reaction with MgO. The presence of these phases will enhance the nucleation potency of the inclusions with respect to graphite. In particular, the (001) basal planes of the crystals are favorable sites for graphite nucleation, since these facets allow for the development of coherent/semicoherent low-energy interfaces between the substrate and the nucleus. In contrast, the fading of inoculation can be explained by a general coarsening of the inclusion population with time, which reduces the total number of catalyst particles for graphite in the melt. A theoretical analysis of the reaction kinetics gives results which are in close agreement with experimental observations.

I. INTRODUCTION

DUCTILE iron is iron-carbon-silicon alloys where the chemical composition is adjusted to ensure that carbon precipitates as graphite spheroids during solidification. One of the most important stages in the iron founding process is the economic production of liquid iron and its treatment in preparation for pouring into the mold. This involves maintaining compositional and temperature control over the liquid during melting in order to achieve the correct composition for the specified iron, the correct graphitization potential, and the correct state of nodularization and inoculation to ensure a sound casting of the desired structure and the required properties.

Magnesium is the most popular spheroidizing agent, and it is usually added in multicomponent alloy form. These components contain additions to reduce reaction violence, promote graphite spheroidization, neutralize the effect of impurities on graphite morphology, and control the matrix structure. The most common alloys for nodularization are ferrosilicon containing 3 to 12 pct magnesium.

Inoculation is a means of controlling the structure and properties of cast iron by minimizing undercooling and increasing the number of graphite nodules during solidification. An inoculant is a material added to the liquid iron just prior to casting that will provide a suitable phase for nucleation of graphite nodules during the subsequent cooling.[1] Traditionally, inoculants have been based on graphite, ferrosilicon, or calcium silicide. The most popular inoculant today is ferrosilicon containing small quantities of elements, such as Ca, Al, Zr, Ba, Sr, and Ti.[2]

It follows from the preceding discussion that a verified quantitative understanding of the graphite formation in ductile cast iron requires detailed information about the reactions occurring during nodularization and inoculation. Consequently, the first part of this investigation is concerned with basic studies of factors controlling the chemical composition, crystal structure, and size distribution of nonmetallic inclusions in such materials. In particular, attempts have been made to correlate changes in the inclusion characteristics with the presence of specific elements in the inoculants (*e.g.*, Ca, Sr, Ba, and Al), utilizing both scanning electron microscopy (SEM) and transmission electron microscopy (TEM).

The second part of this investigation deals with the inoculation mechanisms in ductile cast iron, with particular emphasis on the theoretical aspects of heterogeneous nucleation. There seems to be general agreement that the nucleus/substrate interfacial energy is the controlling factor in heterogeneous nucleation behavior.[3] However, since the total solid/liquid interfacial energy of the system is composed of several contributing factors which cannot readily be accounted for in a simple mathematical treatment of the process, the present analysis is restricted to an assessment of the planar lattice disregistry between graphite and specific inclusion catalyst phases. This concept has proven useful in the past to evaluate the nucleation potency of different types of inoculants in ingots and castings.[4,5,6]

In addition, the microstructure of ductile cast iron is strongly influenced by reactions taking place in the solid state. Consequently, aspects of graphite growth during cooling in the austenite (γ) and austenite + ferrite ($\gamma + \alpha$) regimes are considered in an accompanying article (Part II[7]).

II. A STATE OF THE ART REVIEW

In this section, the conditions for graphite formation in ductile cast iron are discussed in terms of nodularization and inoculation practice and casting procedure.

T. SKALAND, formerly Ph.D. Graduate Student, Division of Metallurgy, The Norwegian Institute of Technology, is Senior Research Metallurgist, Elkem a/s-Research, N-4602 Kristiansand, Norway. Ø GRONG, Professor, and T. GRONG, Professor and Head SINTEF-Metallurgy, are with the Division of Metallurgy, The Norwegian Institute of Technology, 7034 Trondheim, Norway.

Manuscript submitted June 19, 1992.

In particular, the existing theories for the nucleation and growth of graphite nodules in such materials have been critically reviewed in order to establish a firm basis for a future experimental exploration of the system.

A. *Heterogeneous Nucleation Theory*

Heterogeneous nucleation of graphite is an important aspect of cast iron metallurgy.[8] The classic model for heterogeneous nucleation is shown schematically in Figure 1. Here, the graphite phase G grows from the nucleant N and the geometry of the graphite phase is a segment of a sphere of radius r and an angle of contact Θ. The interfacial energies between the three phases, graphite (G), nucleant (N), and liquid (L) are γ_{GN}, γ_{GL}, and γ_{NL}, respectively. The following relationship exists between the interfacial energies:

$$\gamma_{\mathrm{GL}} \cos \Theta + \gamma_{\mathrm{GN}} = \gamma_{\mathrm{NL}} \qquad [1]$$

The change in free energy, ΔG, accompanying the formation of a graphite nucleus with this configuration is given by

$$\begin{aligned} \Delta G &= -V_G \Delta G_V + A_{\mathrm{GL}}\gamma_{\mathrm{GL}} + A_{\mathrm{GN}}\gamma_{\mathrm{GN}} - A_{\mathrm{GN}}\gamma_{\mathrm{NL}} \\ &= f(\Theta)\left(-\frac{4}{3}\pi r^3 \, \Delta G_V + 4\pi r^2 \gamma_{\mathrm{GL}}\right) \end{aligned} \qquad [2]$$

where V_{G} is the volume of solid graphite, ΔG_V is the free energy of graphite formation, A_{GL} and A_{GN} are the area of the graphite-liquid and graphite-nucleant interfaces, respectively, and $f(\Theta)$ is the so-called shape factor, defined as

$$f(\Theta) = \frac{(2 + \cos \Theta)\,(1 - \cos \Theta)^2}{4} \qquad [3]$$

The critical radius of the stable nucleus, r^*, is found by differentiating Eq. [2] with respect to r and equating to zero:

$$r^* = -\frac{2\gamma_{\mathrm{GL}} \sin \Theta}{\Delta G_V} \qquad [4]$$

The corresponding value of the critical free energy barrier, ΔG^*, is then given by

$$\Delta G^* = \frac{16\pi\gamma_{\mathrm{GL}}^3}{3\,\Delta G_V^2} f(\Theta) = \frac{C_1}{(\Delta T)^2} f(\Theta) \qquad [5]$$

where ΔT is the undercooling and C_1 is a kinetic constant which is characteristic of the system under consideration.

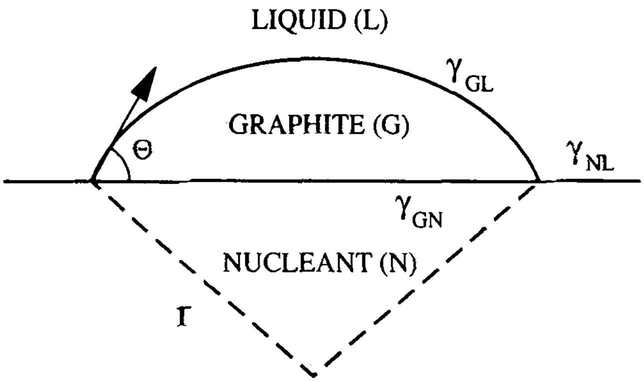

Fig. 1—Schematic representation of heterogeneous nucleation.

When $\Theta = 0$, the graphite nucleus will completely wet the substrate, which implies that there is no energy barrier to nucleation. The nucleation rate $\dot{N}$ (the number of graphite nuclei formed per unit time and volume) is, in turn, inter-related to ΔG^* through the following equation:[2]

$$\dot{N} = \nu N_V \exp\left[-\frac{(\Delta G_D + \Delta G^*)}{kT}\right] \qquad [6]$$

where ν is a frequency factor, N_V is the total number of heterogeneous nucleation sites per unit volume, and ΔG_D is the activation energy for diffusion of atoms across the interface of the nucleus. Since ΔG_D is negligible compared with ΔG^* in liquids, the nucleation rate of graphite is determined by ΔG^*.

The value of ΔG^* (or ΔT) depends, in turn, on the crystallographic disregistry between the substrate and the nucleated solid. The disregistry can be defined as $\delta = (\Delta a_0/a_0)$, where Δa_0 is the difference between the lattice parameter of the substrate and the nucleated solid for a low-index plane and a_0 is the lattice parameter for the nucleated phase. A mean factor representing planar disregistry can be calculated as follows:[4]

$$\delta\,(\mathrm{pct}) = \frac{\delta_1 + \delta_2 + \delta_3}{3} \times 100 \qquad [7]$$

where δ_1, δ_2, and δ_3 are the disregistries calculated along the three lowest index directions within a 90 deg quadrant of the planes of the nucleated solid and the substrate.

In practice, the undercooling, ΔT, increases monotonically with increasing values of the planar lattice disregistry[9] (δ), as shown in Figure 2. Since the undercooling during solidification of ductile cast iron varies typically from 2 to 10 °C[8] (depending on the section size), the results in Figure 2 suggest that the planar lattice disregistry between the inoculant and the graphite

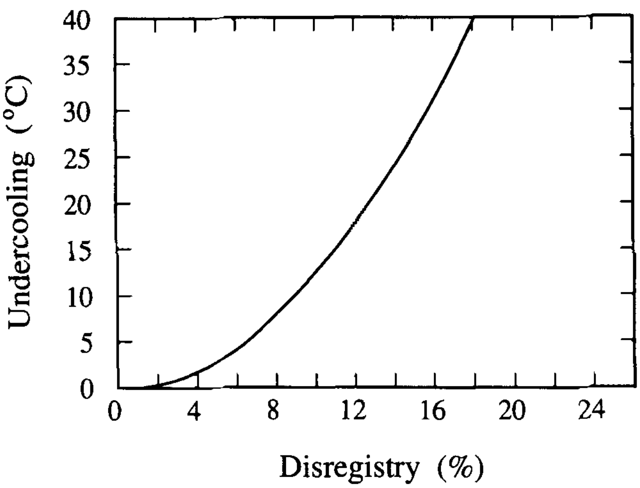

Fig. 2—Characteristic undercooling *vs* planar lattice disregistry.[4]

is of the order of 3 to 10 pct. Such low values are characteristic of coherent/semicoherent interfaces.

B. *Graphite Nucleation Mechanisms*

Traditionally, cast iron inoculants are based on ferrosilicon, graphite, or calcium silicide,[1,10] the former being the most popular. Since pure Si and FeSi alloys are ineffective as inoculants, their nucleation potency depends on the presence of minor elements, such as Ca, Al, Zr, Ba, Sr, and Ti, in the alloys.[11-16] At present, the role of these minor elements is not fully understood.

1. *The graphite theory*

The early theories were based on the assumption that the graphite nucleation occurred epitaxially from other graphite particles contained in the melt.[17] Eash[18] extended these ideas to Si-based inoculants by proposing that their effectiveness is due to the formation of Si-rich regions around the dissolving particles within which the solubility of carbon is sufficiently low to promote graphite precipitation. Later, Feest *et al.*[19] showed that this assumption is not correct, since the dissolution time of ferrosilicon in liquid iron is just a matter of seconds, and that graphite tends to form at the interface between the dissolving particle and the liquid. They therefore modified the model of Eash[18] by proposing that these seed crystals will be preserved in the melt down to the eutectic temperature, provided that Sr or Ba is present in sufficient amounts to prevent redissolution of the graphite.[20]

2. *The silicon carbide theory*

Following the dissolution of ferrosilicon in liquid cast iron, Wang and Fredriksson[21,22] observed that silicon carbide crystals and graphite particles were formed in the melt close to the dissolving ferrosilicon particles. They also observed that these transient particles redissolve readily after the inoculation treatment. No oxide or sulfide particles were detected. Based on their experimental observations, a theory was developed and calculations performed in order to explain the nucleation of graphite and the fading mechanism. A salient assumption in the model of Wang and Fredriksson[21,22] is the existence of an inhomogeneous distribution (local supersaturation) of C and Si in the melt subsequent to the SiC dissolution which provides the necessary driving force for homogeneous nucleation of graphite. The fading effect is thus explained by a homogenization of the melt with respect to silicon and carbon through convection and diffusion.

3. *The salt-like carbide theory*

In a classic article on the nature of the graphite nuclei, Lux[23] considers both homogeneous and heterogeneous nucleation of graphite. He concludes that the elements calcium, strontium, and barium form salt-like carbides of the CaC_2 type in liquid iron and that a direct epitaxial transition from the CaC_2 lattice to the graphite lattice is possible without major changes in the lattice dimensions. Under such conditions, the interfacial energy between the nucleus and the substrate will be sufficiently low to allow for extensive graphite nucleation during solidification.

4. *The sulfide/oxide theory*

Several investigators[24-29] have suggested that graphite nucleation occurs on sulfide, oxide, or nitride particles which are formed after the addition of the inoculant. Lalich and Hitchings[30] confirmed this hypothesis by demonstrating the importance of nonmetallic inclusions. They found that compounds of magnesium calcium sulfide act as nucleation sites for graphite nodules in ductile cast irons treated with magnesium ferrosilicon alloys. They concluded that the majority of nodules in ductile cast iron are associated with nonmetallic inclusions and that graphite growth in some instances is also related to the shape and distribution of these inclusions.

Inclusions in graphite nodules extracted from cast iron have been investigated by different techniques in order to determine the identity of the catalyst particles. These techniques include both electron diffraction pattern analysis and X-ray microanalysis.[31,32,33] An investigation by Jacobs *et al.*[25] was directed to determine the nature of nuclei and detect possible changes in their chemical composition and crystal structure after treatment of iron with magnesium ferrosilicon. The subsequent inoculation treatment included the use of the commercial alloy Superseed. Different series were carried out in order to clarify the effects of elements, such as Al and Sr, on the inclusion characteristics. These results are interesting for cast iron in general, since the examination revealed evidence of a duplex substrate structure consisting of a sulfide core surrounded by an oxide shell. The different constituent phases were as follows:

core (Ca, Mg) sulfide or (Sr, Ca, Mg) sulfide;
outer shell (Mg, Al, Si, Ti) oxide.

Moreover, Jacobs *et al.*[25] observed that inclusions embedded in the iron matrix contained the same constituent elements as those detected in the nodule centers and that the typical size of the particles was about 1 μm. The latter observation shows that the inclusions in ductile cast iron are much smaller than those commonly found in ladle-refined steel.

5. *Graphite nucleation in high-purity melts*

Heterogeneous nucleation of graphite at foreign particles has also been reported in melts containing low levels of sulfur and oxygen (less than 0.2 and 7 ppm, respectively). Dhindaw and Verhoeven[34] studied vacuum-melted high-purity Fe-C-Si alloys produced from ultrapure zone-refined iron. They found from extensive SEM examinations using nondispersive X-ray analysis that impurity atoms were never detected in the nodule centers, which suggests that the graphite nucleation is not associated with sulfide inclusions. However, commercial Si/Ca/Al inoculants effectively increased the nodule count in the ultrapure zone-refined iron from approximately zero to a maximum of about 26 mm^{-2}. Hence, they concluded that the main effect of the calcium-based FeSi inoculant in commercial irons is to promote heterogeneous nucleation of graphite by formation of a metastable carbide (CaC_2), while the corresponding function of the nodularizer is to act as scavenger for sulfur and oxygen to enhance the nodular growth morphology.

It should be noted that a maximum nodule count of about 26 mm^{-2}, as reported by Dhindaw and

Verhoeven,[34] is rather low compared with that normally observed in commercial ductile cast iron where the nodule number density may exceed 300 to 400 mm^{-2}. Consequently, their investigation is not conclusive in that it excludes the possibility of graphite nucleation on nonmetallic inclusions.

C. *Nature of Nonmetallic Inclusions*

Nonmetallic inclusions of varying composition have been observed in the iron matrix and at the centers of graphite nodules by a number of investigators.[24–33] Table I gives a summary of different element combinations and phases detected in the inclusions.

In the periodic table of elements, the group IIA elements Mg, Ca, Sr, and Ba are of specific interest in ductile iron production, since they all are strong sulfide and oxide formers. In the following possible reactions between these elements and sulfur, oxygen, carbon, and silicon will be discussed.

1. *Sulfides*

The pure sulfides of the group IIA elements are all of the face centered cubic NaCl-structure type and are characterized by similar lattice parameters and high melting points. In cast iron melts, these sulfides are among the most stable nonmetallic compounds. Hence, sulfides should form in preference to oxides. This conclusion is in close agreement with the results of Jacobs *et al.*[25] who found that the inclusions consisted of a sulfide core surrounded by an oxide shell. Similar observations have also been made in gray cast irons where sulfur is known to be an essential element for favorable response to inoculation.[19,29] Table II gives a summary of crystal structures, melting points, and standard free energies of formation for the group IIA sulfides.

2. *Carbides*

The carbides CaC_2, SrC_2, and BaC_2 also reveal the NaCl structure type and have similar lattice parameters. They are supposed to be metastable in liquid iron, but it is uncertain whether these phases actually form in ductile cast iron. In fact, the carbides have never been detected experimentally, although they, from a theoretical standpoint, are considered to be favorable nucleation sites for graphite.[23] It is interesting to note that Mg does not form any known compound of the MgC_2 type. This might explain why Mg is only used as a spheroidizing agent in ductile cast iron and not as an inoculant. Table III gives a summary of crystal structures, melting points, and standard free energies of formation for the group IIA carbides.

Table I. Summary of Element Combinations and Phases Detected in Inclusions

Phase	Reference
MgS	30, 35, 36, 37, 38, 39
CaS	30, 35, 36
SrS	36
CeS	37
LaS	37
MgO	38, 39, 40, 41, 42
SiO_2	38, 41, 42, 43
$MgO{\cdot}SiO_2$	38, 42
$2MgO{\cdot}SiO_2$	38, 39, 42
$(Mg, Al)_3O_4$	44
$(Mg, Al)SiO_3$	44
$(Mg, Ca, Al)SiO_3$	44
Fe_2O_3	40, 42
Fe_2SiO_4	45
Mg-Al-Si-Ti-O	36
CeO_2	40
$MgSiN_2$	35
Mg_3N_2	46
Mg_3P_2	46

3. *Oxides*

The group IIA elements also form stable oxides in liquid iron, and nodularizers and inoculants based on these elements are known to be effective deoxidizers. Table IV gives information on crystal structures, melting points, and standard free energies of formation for the pure oxides.

In the following, different types of oxide inclusions which contain Mg, Ca, Sr, or Ba as a constituent element will be considered. Since these elements are added *via* ferrosilicon, the ternary system $XO\text{-}Al_2O_3\text{-}SiO_2$ (X denotes Mg, Ca, Sr, or Ba) provides a convenient basis for the discussion of oxide inclusions in ductile cast iron. Of specific interest in this respect is the $MgO\text{-}Al_2O_3\text{-}SiO_2$ and the $CaO\text{-}Al_2O_3\text{-}SiO_2$ ternary systems, since a variety of different phases (silicates and aluminates) may form, depending on the deoxidation and inoculation practice applied.

4. *The $MgO\text{-}Al_2O_3\text{-}SiO_2$ system*

Nonmetallic inclusions containing MgO as one component may form during the magnesium treatment. The pure $MgO\text{-}Al_2O_3\text{-}SiO_2$ system is similar to the $MnO\text{-}Al_2O_3\text{-}SiO_2$ and $FeO\text{-}Al_2O_3\text{-}SiO_2$ systems.[48] It is evident from these phase diagrams that a number of silicate phases may form as a result of reactions between MgO and SiO_2, including

$$MgO + SiO_2 = MgO{\cdot}SiO_2 \quad \text{(enstatite)} \qquad [8]$$

$$2MgO + SiO_2 = 2MgO{\cdot}SiO_2 \quad \text{(forsterite)} \qquad [9]$$

Enstatite can exist in three different modifications and is a common reaction product in Mg-treated ductile cast iron.[42,48] MgO in $MgO{\cdot}SiO_2$ can be completely substituted by FeO, but pure $FeO{\cdot}SiO_2$ is not stable at normal pressures. MgO can also be replaced by CaO up to about 50 wt pct. In addition, enstatite may dissolve as much as 10 wt pct Al_2O_3. Because of a faceted growth morphology, enstatite tends to form characteristic rectangularly shaped inclusions in ductile cast iron, which means that they can easily be identified by means of optical microscopy.[48]

The other magnesium silicate type, forsterite, may also exist in liquid iron. This phase may contain varying amounts of other oxides in solid solution. For example, CaO is widely soluble in forsterite, since the crystal structure of $2MgO{\cdot}SiO_2$ is similar to that of $\gamma\text{-}2CaO{\cdot}SiO_2$.[48] In addition to enstatite and forsterite, a variety of other phases has been detected in ductile cast iron, including $(Mg, Al)_3O_4$, $(Mg, Al)SiO_2$, and (Mg, Al, Ca)SiO_3 together with complex calcium and aluminum silicates and pure silica.[44]

Table II. Summary of Crystal Structures, Melting Points, and Standard Free Energies of Formation for the Group IIA-Sulphides[47]

Phase	Space Group	Crystal System	Lattice Parameter (Å)	T_M (°C)	ΔG_F* (kJ/mol)
MgS	Fm3m	cubic	5.191	2000	−232
CaS	Fm3m	cubic	5.696	2450	−380
SrS	Fm3m	cubic	6.020	2000	−370
BaS	Fm3m	cubic	6.386	2227	−356

*Standard free energy of formation at 1327 °C (1600 K).

Table III. Summary of Crystal Structures, Melting Points, and Standard Free Energies of Formation for the Group IIA Carbides[47]

Phase	Space Group	Crystal System	Lattice Parameter (Å)	T_M (°C)	ΔG_F* (kJ/mol)
MgC_2	—	—	—	—	—
CaC_2	Fm3m	cubic	5.86	2300	−106
SrC_2	Fm3m	cubic	6.24	—	−93
BaC_2	Fm3m	cubic	6.56	—	−96

*Standard free energy of formation at 1327 °C (1600 K).

5. *The CaO-Al_2O_3-SiO_2 system*

Calcium is from a technical standpoint insoluble in liquid iron. Nevertheless, a small solubility has been reported by Sponseller and Flinn,[49] who found that pure iron could dissolve up to 0.032 wt pct Ca at 1600 °C. Slightly higher values were observed in the presence of aluminum, carbon, nickel, and silicon. Calcium is the most common trace element in ferrosilicon inoculants. Consequently, due to the low solubility and the high affinity to oxygen, calcium could play a role in the graphite nucleation process by entering the deoxidation products at some later stage of the process. However, in steel inclusions, CaO is not present as a separate phase since it reacts readily with other oxides to form complex calcium silicates and aluminates. This is probably also the case in ductile cast iron.

Referring to the CaO-Al_2O_3-SiO_2 phase diagram,[48] CaO can combine with silica according to the following reactions:

$$CaO + SiO_2 = CaO{\cdot}SiO_2 \quad \text{(wollastonite)} \qquad [10]$$

$$3CaO + 2SiO_2 = 3CaO{\cdot}2SiO_2 \quad \text{(rankinite)} \qquad [11]$$

$$2CaO + SiO_2 = 2CaO{\cdot}SiO_2 \quad \text{(bredigite)} \qquad [12]$$

$$3CaO + SiO_2 = 3CaO{\cdot}SiO_2 \quad \text{(alite)} \qquad [13]$$

Several modifications of the calcium silicates are also known, but the transformations between the different polymorphic forms are complex and not fully understood.[48]

$CaO{\cdot}SiO_2$ may dissolve varying amounts of MnO, FeO, and Al_2O_3 but not MgO. Inclusions with a composition corresponding to $CaO{\cdot}SiO_2$ are commonly observed in steel deoxidized with CaSi. These inclusions may contain up to about 10 wt pct Al_2O_3 in solid solution.[48]

CaO can also combine with alumina to form a number of different phases, including[48]

$$CaO + Al_2O_3 = CaO{\cdot}Al_2O_3 \qquad [14]$$

$$CaO + 2Al_2O_3 = CaO{\cdot}2Al_2O_3 \qquad [15]$$

$$CaO + 6Al_2O_3 = CaO{\cdot}6Al_2O_3 \qquad [16]$$

$$3CaO + Al_2O_3 = 3CaO{\cdot}Al_2O_3 \qquad [17]$$

Oxide inclusions containing $CaO{\cdot}Al_2O_3$ and $CaO{\cdot}2Al_2O_3$ are all common deoxidation products. Some of the group IIA silicates and aluminates are summarized in Table V. This table also includes data for the inclusion crystal structures, lattice parameters, and melting points.

Four intermediate ternary phases exist in the ternary CaO-Al_2O_3-SiO_2 system.[48] Their stoiciometric compositions are as follows:

$$CaO{\cdot}Al_2O_3{\cdot}2SiO_2 \quad \text{(anorthite)} \qquad [18]$$

$$2CaO{\cdot}Al_2O_3{\cdot}SiO_2 \quad \text{(gehlenite)} \qquad [19]$$

$$2CaO{\cdot}2Al_2O_3{\cdot}5SiO_2 \quad \text{(corderite)} \qquad [20]$$

$$3CaO{\cdot}Al_2O_3{\cdot}3SiO_2 \quad \text{(grossularite)} \qquad [21]$$

Bruch *et al.*[51,52] have studied the composition of calcium inclusions in steel after CaSi deoxidation. The mean composition of these CaO-containing inclusions was found to be situated within the dotted area of Figure 3. Crystalline ternary phases in the CaO-Al_2O_3-SiO_2 system are rarer than glassy phases. The most common of the crystalline phases is anorthite ($CaO{\cdot}Al_2O_3{\cdot}2SiO_2$) which is the only ternary phase within the dotted area of Figure 3. Anorthite undergoes four different transformations down to room temperature, and the stable high-temperature modification is the

Table IV. Summary of Crystal Structures, Melting Points, and Standard Free Energies of Formation for the Group IIA Oxides[47]

Phase	Space Group	Crystal System	Lattice Parameter (Å)	T_M (°C)	ΔG_F* (kJ/mol)
MgO	Fm3m	cubic	4.215	2832	−401
CaO	Fm3m	cubic	4.811	2927	−466
SrO	Fm3m	cubic	5.140	2665	−428
BaO	Fm3m	cubic	5.539	2013	−395

*Standard free energy of formation at 1327 °C (1600 K).

Table V. Selected Crystallographic and Thermodynamic Data for Some Possible Silicates and Aluminates in Liquid Iron Containing Mg, Ca, Sr, and Ba[47,48,50]

Phase	Space Group	Crystal System	Lattice Parameter (Å)	T_M (°C)	ΔG_F* (kJ/mol)
$MgO{\cdot}SiO_2$	Pbca	orthorhombic	18.2/8.86/5.204	1577	−1060
$CaO{\cdot}SiO_2$	P1	hexagonal	6.82/19.65	1125–1544	−1184
$SrO{\cdot}SiO_2$	—	hexagonal	7.127/10.115	1580	−1186
$BaO{\cdot}SiO_2$	—	hexagonal	7.500/10.467	1605	−1180
$MgO{\cdot}Al_2O_3{\cdot}2SiO_2$	—	—	—	—	—
$CaO{\cdot}Al_2O_3{\cdot}2SiO_2$	$P6_3/mcm$	hexagonal	5.113/14.743	1550	−3022
$SrO{\cdot}Al_2O_3{\cdot}2SiO_2$	—	hexagonal	5.25/7.56	—	—
$BaO{\cdot}Al_2O_3{\cdot}2SiO_2$	—	hexagonal	5.304/7.789	(1380)	—
$MgO{\cdot}6Al_2O_3$	—	—	—	—	—
$CaO{\cdot}6Al_2O_3$	—	hexagonal	5.54/21.82	1850	—
$SrO{\cdot}6Al_2O_3$	$P6_3/mmc$	hexagonal	5.589/22.07	1500	—
$BaO{\cdot}6Al_2O_3$	$P6_3/mmc$	hexagonal	5.607/22.90	(1400)	—
$2MgO{\cdot}SiO_2$	Pmnb	orthorhombic	4.76/10.20/5.99	1898	−1491

*Standard free energy of formation at 1327 °C (1600 K).

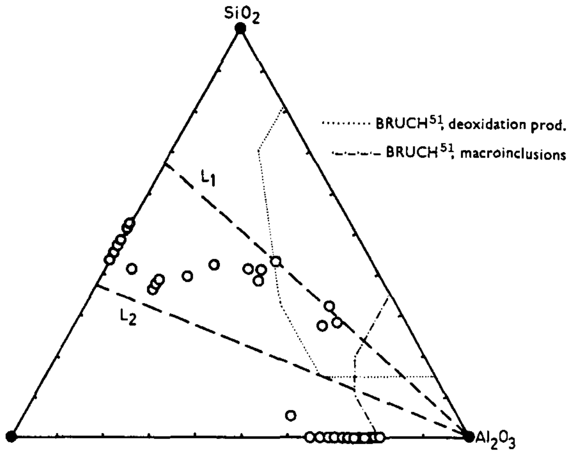

Fig. 3 — Summary of the mean composition (in weight percent) of different calcia containing inclusions found in steel after CaSi deoxidation.[48]

hexagonal α-anorthite. Crystallographic data and melting point for the α-anorthite phase are given in Table V. Note that crystalline ternary phases of the gehlenite, corderite, and grossularite type are not common deoxidation products in liquid steel or cast iron.

6. *Phases containing Mg, Ca, Sr, and Ba*

This section gives a summary of some possible oxide inclusions in liquid iron. The phases most likely to form are listed in Table V. As mentioned in Section II–C–5, calcium is not present as pure CaO since it reacts readily with other components in the melt. When ferrosilicon dissolves in liquid iron, wollastonite may form as a result of reactions between CaO and Si:[53]

$$3CaO\ (s) + \underline{Si} = 2Ca\ (g) + CaO{\cdot}SiO_2\ (s) \qquad [22]$$

If MgO is present in the melt prior to the calcium/silicon addition, the following reaction is thermodynamically feasible:[53]

$$2MgO\ (s) + CaO\ (s) + \underline{Si} = 2Mg\ (g) + CaO{\cdot}SiO_2\ (s) \qquad [23]$$

When MgO is present as a silicate, a slightly different reaction may occur:[53]

$$MgO{\cdot}SiO_2\ (s) + Ca\ (l) = Mg\ (g) + CaO{\cdot}SiO_2\ (s) \qquad [24]$$

An interesting observation is that the group IIA elements Ca, Sr, and Ba all tend to form carbides, silicates, and aluminates of similar crystal structures. In contrast, magnesium does not form these types of phases, as shown by the data in Tables III and V.

D. *Graphite Growth Mechanisms*

Graphite is the first phase to form in hypereutectic irons during solidification. It has a high entropy of fusion, and growth is controlled by the rate at which different solid-liquid interface structures can incorporate atoms. The resulting hexagonal crystal structure is bound by six prism faces and two close-packed basal faces, as shown in Figure 4.

It is proposed that growth normally occurs along the pole of the plane with the lowest interfacial energy in contact with the melt. This means that the normal graphite growth direction should lie along the pole of the basal plane in the absence of surface-active elements, thus resulting in nodular graphite growth. This behavior has been observed in vacuum-melted high-purity melts.[54] When surface-active elements (*e.g.*, oxygen, sulfur, *etc.*) are present, they are preferentially absorbed onto the high energy prism planes, thus reducing the prism plane interfacial energy with the melt to a value below that of the basal planes. This results in a change in growth direction to the pole of the planes with the lowest interfacial energy, *i.e.*, the prism planes.[55]

In the absence of surface-active elements, carbon atoms are preferentially added to the basal planes. This growth in the *c* direction occurs from the step of screw dislocations intersecting the interface.[56] The step of a screw dislocation becomes a spiral during growth, as shown in Figure 5. Atoms attach at the step of the spiral, and the resulting rotation produces growth of one step height per revolution. The low-energy basal plane propagates along its pole and produces the lowest free energy melt-graphite configuration. Figure 6 shows the branching of graphite crystals by an extension of the *c*-axis resulting in a graphite spherulite.

Surface-active elements may be absorbed on the high-energy prism plane to reduce the interfacial energy with the melt to a value below that of the basal plane. When this occurs, the growth rate along the prism pole exceeds that along the basal pole, thus resulting in flake graphite growth.

The function of the nodularizer (*e.g.*, Mg, Ce, *etc.*) is to neutralize surface-active elements capable of preferentially absorbing on the graphite prism plane. The list of subversive elements includes oxygen, sulfur, lead, tellurium, and possibly others.

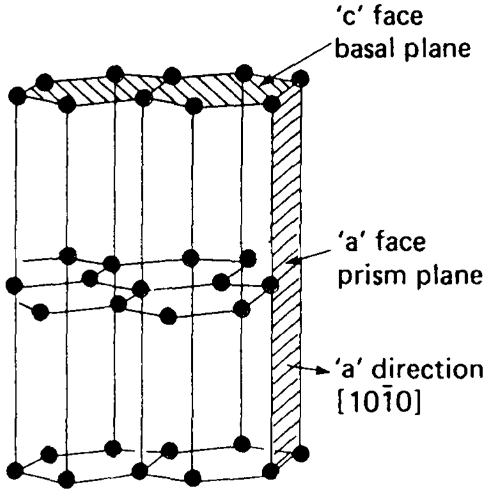

Fig. 4—The graphite crystal structure.[2]

III. EXPERIMENTAL PROCEDURES

A. *Materials and Casting Performance*

In the present investigation, special heats of high-purity cast iron (75 kg batches) were produced in an induction furnace. The iron was superheated to approximately 1510 °C before tapping into the treatment ladle. The liquid metal was magnesium treated with a 4.5 pct magnesium-containing ferrosilicon alloy, using a conventional sandwich method. The subsequent stream inoculation was carried out with various inoculants immediately before casting into the sand molds. The dimensions of the castings were 50 × 120 mm with section sizes of 5, 10, 15, 20, and 30 mm, respectively, as shown in Figure 7. The chemical composition of the charge materials and treatment alloys is given in Table VI, while Table VII contains information on the various combinations of Mg-treatment alloys and inoculants used in the present investigation. Table VIII gives the full chemical composition of the experimental castings, including the gross weight of the charge materials.

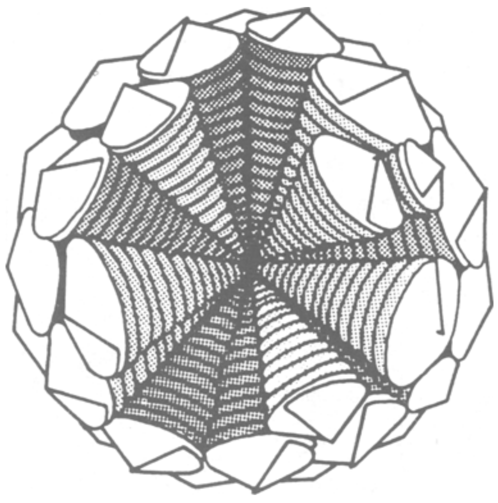

Fig. 5—Graphite spherulite growth obtained from numerous close-packed spirals radiating from a common center.[57]

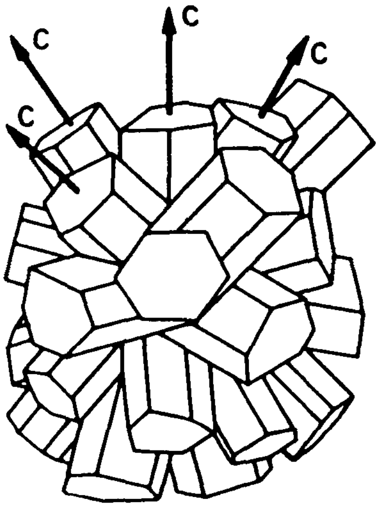

Fig. 6—Star-like branching of a graphite spherulite.[58]

Table VI. Chemical Composition of Charge Materials and Treatment Alloys (Balance: Iron)

Material	Pct C	Pct Si	Pct Mn	Pct P	Pct S	Pct Mg	Pct Al	Pct Ca	Other
Pig iron	4.31	0.17	0.008	0.025	0.003	—	—	—	—
Steel	0.01	0.01	0.02	0.005	0.012	—	0.001	—	—
75 pct FeSi	0.01	76.5	0.09	0.008	—	0.006	0.028	0.006	—
Mg-FeSi A	—	45.5	—	—	—	4.55	0.60	0.75	—
Mg-FeSi B	—	44.7	—	—	—	4.65	0.51	0.015	—
Mg-FeSi C	—	45.2	—	—	—	4.64	0.54	0.92	—
Mg-FeSi D	—	44.8	—	—	—	4.69	0.56	1.86	—
(Ca, Al)-FeSi	—	71.6	0.11	—	—	0.22	0.41	0.88	—
(Sr, Al)-FeSi	—	78.1	0.073	0.017	—	0.026	0.260	0.013	0.851 Sr
(Ca, Ba, Al)-FeSi	—	76.2	0.18	0.014	—	—	0.84	0.92	1.050 Ba
Pure FeSi	0.01	76.5	0.09	0.008	—	0.006	0.028	0.006	—
Al-FeSi	—	75.0	0.10	—	—	0.011	0.33	0.020	—
Ca-FeSi	—	74.1	0.10	—	—	0.021	0.042	0.52	—
Sr-FeSi	—	74.9	0.103	0.009	—	0.005	0.051	0.076	0.603 Sr

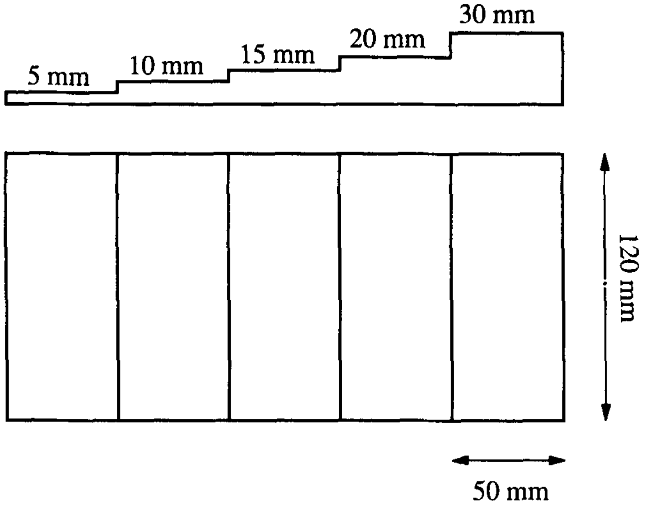

Fig. 7—Geometry of stepped castings.

B. *Optical Microscopy*

Standard metallographic techniques were employed to reveal the graphite nodule distribution and matrix phases. The volume fraction of the different microconstituents (*i.e.*, graphite, ferrite, pearlite, and carbide) was obtained from a series of point counts carried out in a light microscope. The two-dimensional (2-D) number density of graphite nodules was determined from planimetric measurements, using ordinary polished specimens (1-μm diamond paste finish). A total number of approximately 1200 particles were counted in each case. These data were subsequently transformed into three-dimensional (3-D) densities using the Saltykov analysis.[59] The metallographic specimens used in these examinations were taken from the middle of each section size in order to obtain comparable microstructural data in each case.

C. *Preparation of Samples for Scanning Electron Microscopy and Scanning Transmission Electron Microscopy*

The basic inclusion analyses were carried out on quenched samples (weight: 60 g) which were extracted from the melt immediately after the alloy addition. These samples were chilled in a large copper mold to achieve the highest possible cooling rate. In the SEM examinations, ordinary mechanically polished specimens were employed (1-μm diamond paste finish), whereas the scanning transmission electron microscopy (STEM) examinations involved the use of carbon extraction replicas only. The carbon extraction replicas were prepared by depositing a thin layer of carbon (20- to 30-nm thick) onto polished metal samples under high vacuum conditions. The replicas were removed from the metal surface by etching in a 20 pct nital solution (methanol based) and subsequently placed on small copper grids which were inserted into the STEM specimen holder.

Table VII. Combinations of Mg-Treatment Alloys and Inoculants Used in the Experimental Series

Cast Number	Mg-FeSi*	Inoculant
1	A	(Ca, Al)-FeSi
2	A	(Sr, Al)-FeSi
3	A	(Ca, Ba, Al)-FeSi
4	B	(Sr, Al)-FeSi
5	C	(Sr, Al)-FeSi
6	D	(Sr, Al)-FeSi
7	B	—
8	D	—
9	B	Pure FeSi
10	A	Al-FeSi
11	A	Ca-FeSi
12	A	Sr-FeSi

*The notations A, B, C, and D refer to the Mg-FeSi alloys in Table VI.

D. *SEM Inclusion Analysis*

The SEM inclusion examinations were carried out with a JEOL 840 scanning electron microscope equipped with an energy dispersive X-ray unit (EDAX) for microanalysis. The experimental procedure involved both secondary electron imaging and X-ray microanalysis of single particles located in graphite nodules and the iron matrix to determine the approximate size distribution

Table VIII. Chemical Composition of the Cast Materials (Balance: Iron)

Number	Pct C	Pct Si	Pct Mn	Pct P	Pct S	Pct Cr	Pct Ni	Pct Cu	Pct Mo	Pct Nb	Pct Ti	Pct Sn	Pct Mg	Pct Ca	Pct O	Other
1	3.62	2.39	0.02	0.031	0.003	0.02	0.06	0.02	0.01	0.001	0.010	0.007	0.047	0.0021	0.0034	—
2	3.44	2.55	0.03	0.042	0.004	0.03	0.06	0.02	0.01	0.001	0.012	0.007	0.042	0.0019	0.0072	—
3	3.80	2.35	0.06	0.052	0.004	0.03	0.05	0.02	0.01	0.002	0.015	0.009	0.064	0.010	0.003	0.0004 Ba
4	3.57	2.44	0.02	0.033	0.003	0.03	0.06	0.02	0.01	0.001	0.010	0.006	0.033	0.0014	0.0027	—
5	3.67	2.32	0.02	0.033	0.004	0.02	0.06	0.02	0.01	0.001	0.011	0.005	0.046	0.0021	0.0032	—
6	3.72	2.64	0.02	0.028	0.003	0.03	0.06	0.02	0.01	0.001	0.010	0.007	0.047	0.0025	0.0020	—
7	3.48	2.41	0.03	0.033	0.004	0.03	0.06	0.02	0.01	0.001	0.012	0.009	0.046	0.0007	0.0048	—
8	3.54	2.41	0.05	0.021	0.003	0.04	0.06	0.02	0.01	0.002	0.013	0.005	0.054	0.005	0.0019	—
9	3.43	2.24	0.04	0.040	0.003	0.03	0.05	0.01	0.01	0.001	0.009	0.007	0.045	0.0011	0.0040	—
10	3.43	2.49	0.06	0.036	0.002	0.04	0.06	0.02	0.01	0.002	0.018	0.006	0.054	0.007	0.0023	—
11	3.65	2.55	0.05	0.031	0.002	0.04	0.06	0.02	0.01	0.003	0.019	0.008	0.045	0.006	0.0019	—
12	3.43	2.51	0.03	0.049	0.003	0.03	0.05	0.02	0.01	0.003	0.015	0.010	0.040	0.0011	0.0027	—

*Basic charge weight of materials—iron: 67.5 kg; steel: 4.8 kg; FeSi: 1.4 kg; and MgFeSi: 1.3 kg.

and chemical composition of the inclusions. To obtain the required degree of accuracy in the measurements, a minimum of 100 particles were analyzed in each case.

E. *STEM/TEM Inclusion Analysis*

The STEM inclusion analysis was carried out with a PHILIPS* CM 30 scanning transmission electron microscope, provided with an EDAX for microanalysis. The experimental procedure involved digital bright-field imaging, X-ray imaging, and electron diffraction pattern analyses of isolated particles on carbon extraction replicas to reveal details of the different inclusion constituent phases. Additional information on the inclusion crystal structures was obtained from measurements carried out with a JEOL 200CX scanning transmission electron microscope. In the latter case, the inclusion constituent phases were analyzed and identified from electron diffraction patterns and X-ray microanalyses.

IV. RESULTS AND DISCUSSION

A. *Inclusion Characteristics*

1. *Inclusion classification*

It is evident from the SEM micrographs in Figure 8 that the cast iron inclusions can be divided into three main categories:

- type A inclusions, which contain Mg, Ca, S, and Si as the main constituent elements;
- type B inclusions, which contain Mg and Si as the main constituent elements; and
- type C inclusions, which contain Mg, P, and rare earth metals (*e.g.*, Ce or La) as the main constituent elements.

It follows from Figure 8 that inclusions of type A are mainly angular or faceted particles located at the center of the graphite nodules as well as in the iron matrix. Inclusions of type B are rectangular particles which appear mainly in the iron matrix. Finally, inclusions of type C are large, irregularly shaped particles located in the interdendritic regions of the iron. The latter group probably stems from reactions between dissolved magnesium and phosphorus during solidification and is therefore of minor interest in the present context. Table IX gives the relative frequency of the different inclusion classes in the various castings. On the average, they contain approximately 60 pct type A inclusions, 20 pct type B inclusions, and 20 pct type C inclusions.

2. *Elements and phases in type A inclusions*

The presence of silicon and sulfur along with magnesium and calcium in the type A inclusions after nodularization suggests that they are of a heterogeneous chemical nature. The TEM bright-field image in Figure 9(a) reveals evidence of a duplex structure with a sulfide core and a faceted outer shell, similar to that reported previously by Jacobs *et al.*[25] Moreover, the dark-field image in Figure 9(b) indicates the existence of a substructure within the inclusions, which gives rise to a rather complex diffraction pattern due to overlap of matrix reflections from different zone axes. A closer examination of these particles in STEM shows that the sulfide core consists of magnesium, calcium, and sulfur (probably in the form MgS and CaS), while the outer shell mainly contains magnesium and silicon. In view of the previous discussion, it is reasonable to assume that the latter phase is a complex orthorhombic magnesium silicate of the enstatite ($MgO \cdot SiO_2$) or forsterite ($2MgO \cdot SiO_2$) type.

After inoculation with (Ca,Al)-containing ferrosilicon, both calcium and aluminum along with silicon tend to concentrate at the surface of the inclusions, as shown by the STEM X-ray images in Figure 10. These X-ray maps provide valuable qualitative information about the element distribution but are not suitable for quantitative readings (*e.g.*, they cannot be used for assessment of the silicon content in the center of the inclusions). An analysis of the resulting diffraction pattern in Figure 11 shows that this phase conforms to the hexagonal silicate phase anorthite ($CaO \cdot Al_2O_3 \cdot 2SiO_2$) with lattice parameters $a_0 = 5.11$ Å and $c_0 = 14.74$ Å. In Tables X and XI, the measured lattice plane spacings and angles between lattice planes are compared with the reported data for the anorthite phase.

Since the other group IIA elements Sr and Ba form the same types of oxides in ductile cast iron, inoculation with these elements, along with aluminum and silicon, would be expected to promote the formation of the hexagonal phases $SrO \cdot Al_2O_3 \cdot 2SiO_2$ or $BaO \cdot Al_2O_3 \cdot 2SiO_2$ at the surface of the inclusions analogous to that documented earlier for calcium. Unfortunately, the group IIA

---

*PHILIPS is a trademark of Philips Instruments.

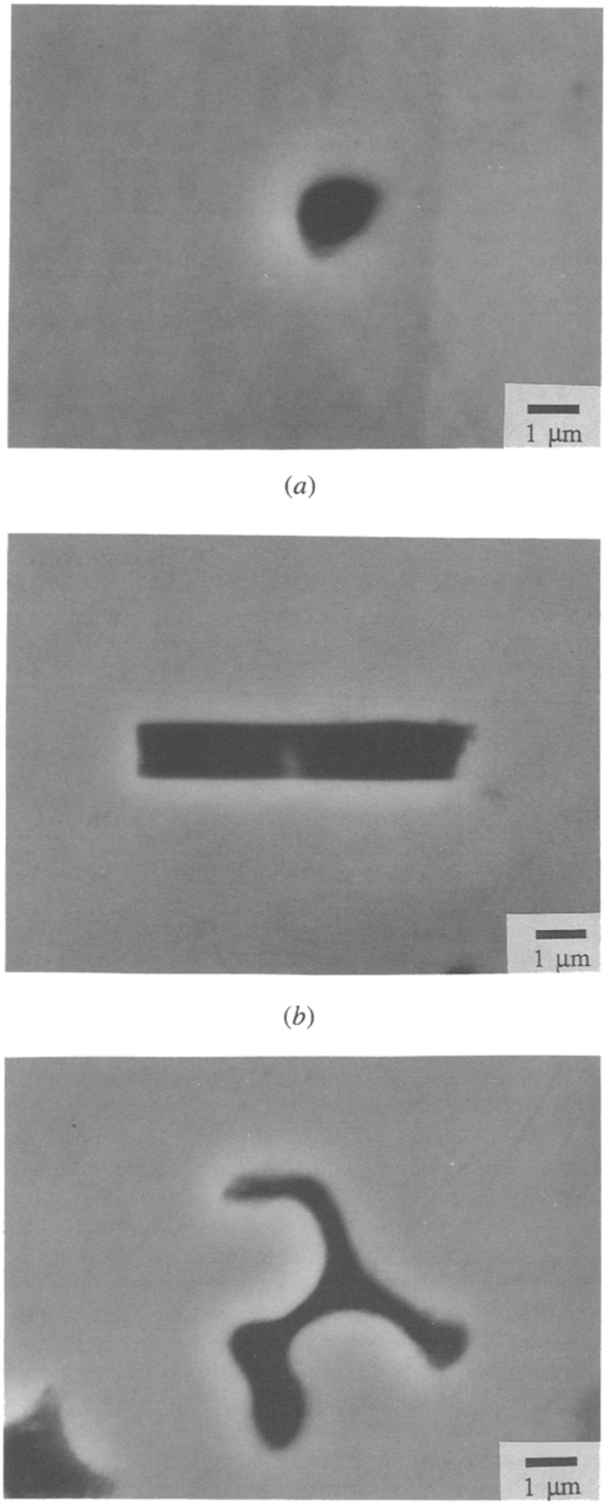

Fig. 8—SEM micrographs of characteristic inclusion morphologies in ductile cast iron: (*a*) type A inclusion containing Mg, Ca, S, and Si; (*b*) type B inclusion containing Mg and Si; and (*c*) type C inclusion containing Mg and P.

Table IX. Relative Frequency of Type A, B, and C Inclusions in Experimental Castings (in Percent)

Casting	Type A	Type B	Type C
No. 1	64	13	23
No. 2	56	28	16
No. 3	48	9	43
No. 4	45	31	24
No. 5	57	19	24
No. 6	63	19	18
No. 7	68	12	20
No. 8	61	8	31
No. 9	62	18	20
No. 10	52	22	26
No. 11	71	11	18
No. 12	60	30	10

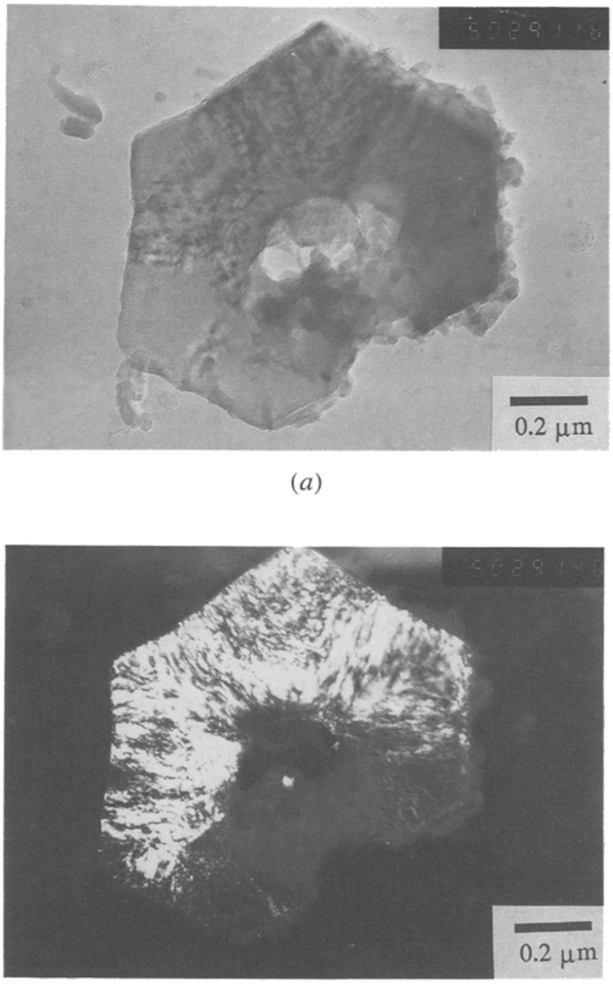

Fig. 9—TEM examination of type A inclusion extracted from casting no. 2: (*a*) bright-field image and (*b*) dark-field image.

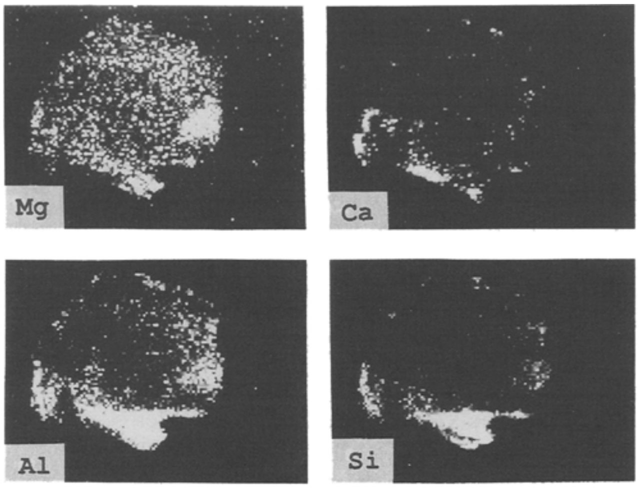

Fig. 10—STEM X-ray images showing the distribution of Mg, Ca, Al, and Si in type A inclusion after inoculation with a (Ca,Al)-containing ferrosilicon. The inclusion is extracted from casting no. 1.

inoculant trace elements Ca, Sr, and Ba respond differently to energy dispersive X-ray microanalysis in SEM or STEM. The two extreme elements with respect to atomic number, calcium and barium, can readily be identified by their K_α and L_1 peaks, respectively, in the X-ray spectra. In contrast, the intermediate element strontium is more difficult to trace, since the L_1-Sr peak coincides with the K_α peak for silicon which normally is present in the inclusions. Hence, strontium in the form of $SrO{\cdot}Al_2O_3{\cdot}2SiO_2$ at the surface of the inclusions cannot be detected by means of conventional EDAX analysis.

Table X. Lattice Plane Spacings (d_{hkl}) for the Hexagonal $CaO{\cdot}Al_2O_3{\cdot}2SiO_2$ Phase Compared with Measured Plane Spacings (d_{exp}) from the Diffraction Pattern

hkl	d_{hkl} (Å)	d_{exp} (Å)
$011/1\bar{1}1$	4.24	4.21
012	3.80	3.70

Table XI. Angles between Lattice Planes (Θ_{hkl}) for the Hexagonal $CaO{\cdot}Al_2O_3{\cdot}2SiO_2$ Phase Compared with Measured Angles (Θ_{exp}) from the Diffraction Pattern

$h_1k_1l_1/h_2k_2l_2$	Θ_{hkl}	Θ_{exp}
011/102	56	55
$011/\bar{1}1\bar{1}$	68	70

Since barium is more easy to identify than strontium, casting no. 3, which is inoculated with (Ca,Ba,Al)-containing ferrosilicon, has been subjected to a more thorough examination by SEM. In this particular casting, the addition of the inoculant is four times higher

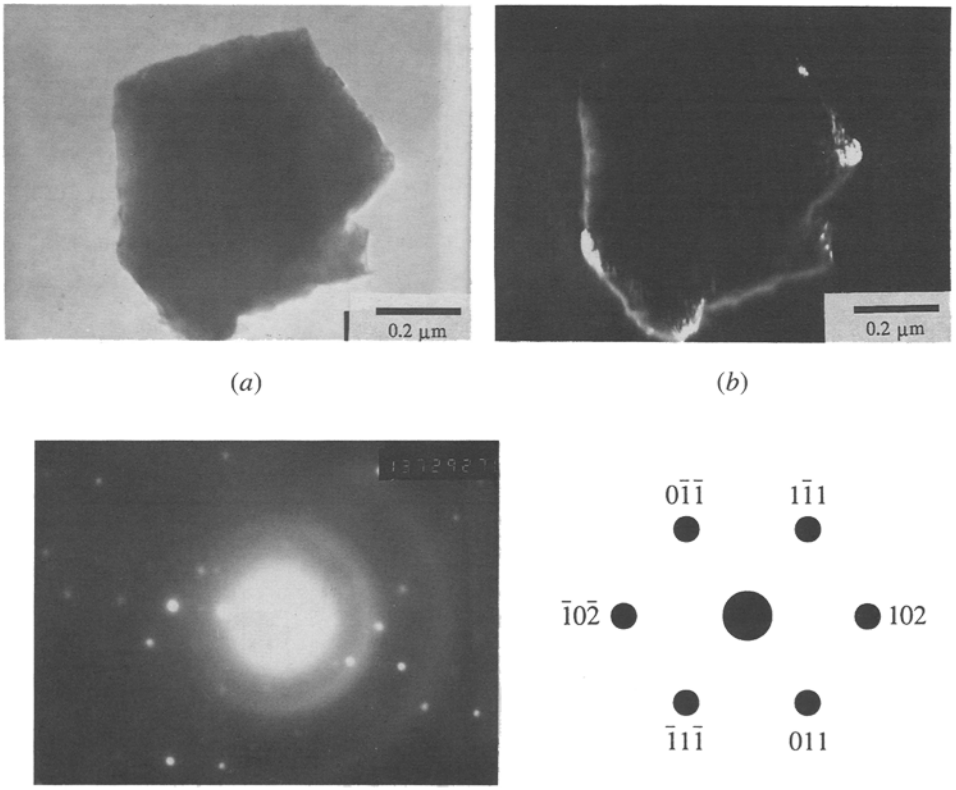

(*a*) (*b*)

(*c*) (*d*)

Fig. 11—TEM examination of type A inclusion in Figure 10: (*a*) bright-field image; (*b*) dark-field image; (*c*) electron diffraction pattern, and (*d*) interpreted diffraction pattern.

than that normally employed (1 wt pct of the total charge) to increase the possibility of detecting the minor elements calcium and barium in the inclusions. Table XII shows the distribution of elements in type A inclusions immediately after nodularization and inoculation.

As expected, the overall chemistry of the inclusions is not significantly affected by the addition of the (Ca,Ba,Al)-containing inoculant. However, in 18 pct of the inclusions, traces of barium can be found along with magnesium, calcium, sulfur, and silicon. This shows that both barium and calcium are capable of modifying the inclusion surface chemistry through an exchange reaction with magnesium.

3. *Elements and phases in type B inclusions*

Apart from the difference in morphology, the distinction between type A and B inclusions lies primarily in their chemical composition. In the latter case, Mg and Si are the dominating constituent elements, while the former type also contains Ca and S. This suggests that the type B inclusions are pure magnesium silicates (probably $MgO \cdot SiO_2$) which form during the primary deoxidation stage following the magnesium treatment.

4. *Inclusion number density and size distribution*

Key results from the inclusion size distribution measurements are summarized in Table XIII for the as-cast 30-mm section size materials. Examples of measured inclusion histograms are given in Figures 12 and 13. It is evident from these data that the majority of the 2-D inclusion diameters fall within a range of 0.4 to 2.0 μm (irrespective of choice of nodularizer and inoculant), with a well-defined peak in the particle frequency at about 1.1 μm. Based on the Fullman's theory[60] for a polydispersed system of spheres, the measured 2-D diameters (d_A) can be converted into 3-D values (d_v) through the following relation:

$$d_v = \frac{\pi}{2} \cdot d_A \qquad [25]$$

From Eq. [25], it is possible to estimate the total number of particles per unit volume (N_v) when the inclusion volume fraction is known. The latter parameter can be obtained from simple stoichiometric calculations by converting the analytical sulfur and oxygen contents (given in Table VIII) to an equivalent inclusion volume, according to the procedure described by Franklin.[61] If it is assumed that all sulfur and oxygen are tied up as magnesium sulfide and complex magnesium silicates,

Table XII. Distribution of Elements in Type A and B Inclusions after Nodularization and Subsequent Inoculation with (Ca, Ba, Al)-Containing Ferrosilicon (Quenched Samples) (The Samples Are Taken from Casting Number 3)

	Frequency (in percent)*					
Sample	Mg	Ca	Si	Al	S	Ba
Nodularized	98	78	78	47	96	—
Nodularized and inoculated	99	90	100	39	99	18

*The numbers refer to the fractions of inclusions which contain a specific element.

Table XIII. Inclusion Data for the As-Cast 30-mm Section Size Materials

Casting	d_A (μm)	d_V (μm)	V_V (cal)	N_V (mm^{-3})
No. 1	1.2	1.9	3.0×10^{-4}	8.5×10^4
No. 2	1.1	1.7	5.4×10^{-4}	2.1×10^5
No. 3	1.1	1.8	3.3×10^{-4}	1.1×10^5
No. 4	1.1	1.7	2.7×10^{-4}	1.1×10^5
No. 5	1.1	1.7	3.4×10^{-4}	1.3×10^5
No. 6	1	1.6	2.4×10^{-4}	1.1×10^5
No. 7	1	1.5	4.2×10^{-4}	2.4×10^5
No. 8	1	1.6	2.3×10^{-4}	1.1×10^5
No. 9	1	1.5	3.3×10^{-4}	1.9×10^5
No. 10	1.1	1.8	2.0×10^{-4}	6.8×10^4
No. 11	1	1.6	1.9×10^{-4}	8.7×10^4
No. 12	1.1	1.8	2.7×10^{-4}	8.9×10^4

d_A: arithmetic mean 2-D inclusion diameter; d_V: arithmetic mean 3-D inclusion diameter; V_V (cal): inclusion volume fraction; and N_V: number of particles per unit volume.

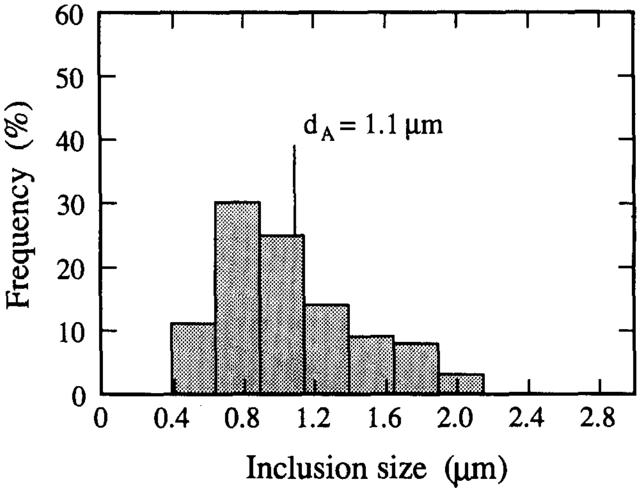

Fig. 12—2-D size distribution of inclusions in casting no. 5 (30-mm section size material).

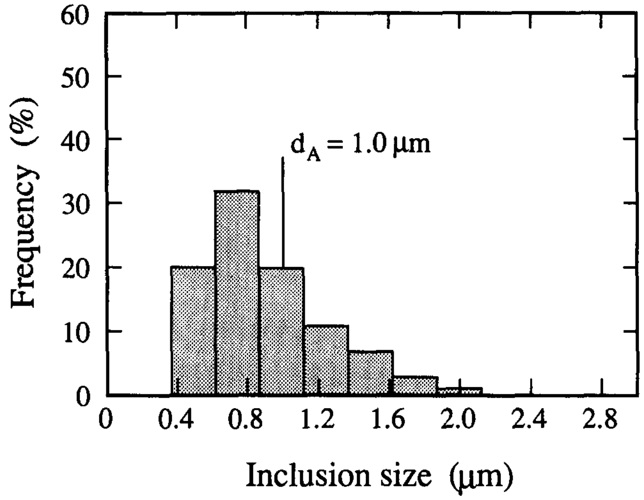

Fig. 13—2-D size distribution of inclusions in casting no. 7 (30-mm section size material).

respectively, the following relationship is obtained for the inclusion volume fraction, V_v(cal):

$$V_v(\mathrm{cal}) \approx 10^{-2} \cdot [4.6\ (\mathrm{wt\ pct\ S}) + 4.9\ (\mathrm{wt\ pct\ O})] \qquad [26]$$

The total number of particles per unit volume (N_v) is then given by

$$N_v = \frac{6V_v}{\pi (d_v)^3} \qquad [27]$$

It is seen from Table XIII that the calculated values for N_v fall within the range from 6.8×10^4 to 2.4×10^5 particles per mm^3. This range in the inclusion density is approximately one order of magnitude higher than the total number of grafite nodules per mm^3 in the as-cast materials (Tables XVII and XVIII).

Table XIV compares data for d_v, V_v, and N_v in quenched samples taken from the melt immediately after nodularization and inoculation of casting no. 3 with corresponding inclusion data for the as-cast 30-mm section size material. It is evident that a slight coarsening of inclusions occurs within the time interval between inoculation and solidification (of the order of 7 minutes). This, in turn, results in a reduction in the inclusion number density from about 4.6×10^5 per mm^3 to approximately 1.1×10^5 per mm^3 if we assume that the volume fraction of inclusions remains constant during the coarsening process.

5. *Nature of inclusion in ductile cast iron*

Based on the results obtained in the previous sections, it is possible to sketch the sequence of reactions occurring during nodularization and inoculation of ductile cast iron as follows.

After nodularization, both magnesium and calcium containing sulfides and silicates can form. The indications are that the oxide phase (*e.g.*, $MgO \cdot SiO_2$) may contain considerable amounts of Al_2O_3 in solid solution. In addition, some aluminum can enter the deoxidation products by formation of more complex phases along with magnesium or silicon (*e.g.*, $MgO \cdot Al_2O_3$ or $MgO \cdot Al_2O_3 \cdot SiO_2$).

The characteristic duplex structure of the type A inclusions (with a sulfide core and an oxide shell) reflects the fact that in cast iron melts, the sulfides are more stable than the oxides,[62] thus promoting sulfide precipitation in preference to oxide formation. Since both magnesium and calcium are among the strongest sulfide formers in cast iron, it is reasonable to assume that these sulfides precipitate homogeneously in the melt immediately after the addition of the nodularizer. The sulfide particles subsequently act as heterogeneous nucleation sites for the oxides, resulting in the characteristic duplex inclusion structure, as shown in Figure 9(a). Moreover, the existence of a substructure within the oxide shell (Figure 9(b)) indicates that the type A inclusions contain different constituent phases. According to the binary MgO-SiO_2 phase diagram, enstatite ($MgO \cdot SiO_2$) can coexist with forsterite ($2MgO \cdot SiO_2$) over a relatively wide composition range.[63] Since both enstatite and forsterite are known to develop faceted crystals of the shape shown in Figure 9(a),[63] it is reasonable to assume that these oxides are the main constituent phases in the type A inclusions along with MgS and CaS.

Table XIV. Changes in the Inclusion Characteristics after Nodularization, Inoculation, and Solidification (Casting Number 3)

Sample	d_V (μm)	V_V (cal)	N_V (mm^{-3})
Nodularized	1.1	3.3×10^{-4}	4.6×10^5
Nodularized and inoculated	1.1	3.3×10^{-4}	4.6×10^5
As-cast	1.8	3.3×10^{-4}	1.1×10^5

In contrast, the rectangular-shaped type B inclusions are presumably single-phase particles of enstatite ($MgO \cdot SiO_2$), as documented previously by Kiessling and Lange.[48] These oxides probably precipitate homogeneously during the primary deoxidation stage due to the lack of potent MgS and CaS catalyst particles in the melt. Growth of the stable nuclei will then occur in a faceted manner because of anisotropy in the growth rate between different crystallographic planes. Figure 14 shows schematic drawings of the three types of inclusions which form after magnesium treatment of ductile cast iron.

6. *Reactions during inoculation*

After inoculation with Ca-, Ba- or Sr-containing ferrosilicon, the type A (and B) inclusions will slightly change their chemical composition due to the formation of new reaction products at the surface of the inclusions. The formation of such complex silicates can occur either as a result of reactions between Ca, Sr, or Ba and dissolved oxygen and silicon in the liquid iron or by an exchange reaction with magnesium, as discussed in Section II–C. In the latter case, we may write

$$MgO \cdot SiO_2\ (s) + \underline{X} = XO \cdot SiO_2\ (s) + \underline{Mg} \qquad [28]$$

$$2(2MgO \cdot SiO_2) + \underline{X} + 2\underline{Al} = XO \cdot Al_2O_3 \cdot 2SiO_2 + 4\underline{Mg} \qquad [29]$$

where X denotes either Ca, Sr, or Ba.

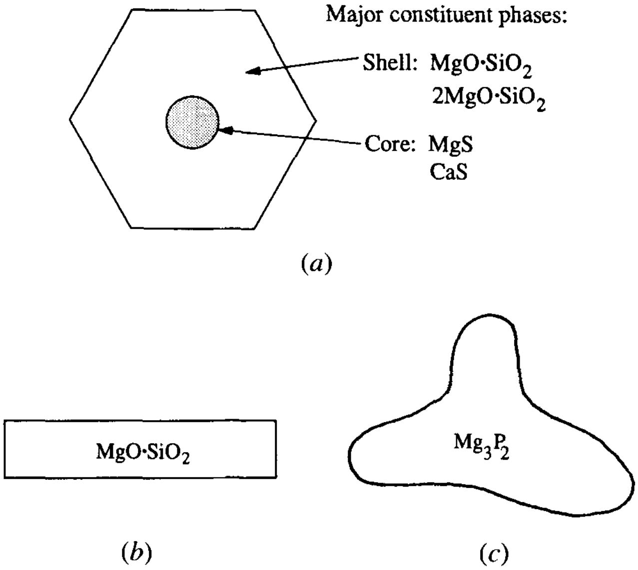

Fig. 14—Major constituent phases in type A, B, and C inclusions after nodularization (schematic): (*a*) type A inclusion; (*b*) type B inclusion; and (*c*) type C inclusion.

As shown in Figure 15, the $XO\cdot SiO_2$ phases may form at the surface of both type A and B inclusions, provided that Ca, Sr, or Ba is added in sufficient amounts through the inoculant. In contrast, formation of $XO\cdot Al_2O_3\cdot 2SiO_2$ is mainly associated with type A inclusions and is contingent upon the existence of free aluminum in the melt. This explains why, for instance, anorthite ($CaO\cdot Al_2O_3\cdot 2SiO_2$) is present at the surface of type A inclusions in casting no. 1 after inoculation with (Ca,Al)-containing ferrosilicon (Figures 10 and 11). Considering the fact that the different silicates of Ca, Sr, and Ba, both the $XO\cdot SiO_2$ and the $XO\cdot Al_2O_3\cdot 2SiO_2$ type, are all phases which will enhance the graphite formation during solidification (Section IV–B), it is not surprising to find that the majority of commercial inoculants for ductile cast iron contain aluminum (normal content between 0.5 and 1 wt pct Al).

7. *Coarsening of inclusions*

The data in Table XIV show that significant coarsening of the inclusions occurs within the time interval between inoculation and solidification.

In general, there are three major inclusion growth processes:[64] (1) collision, (2) diffusion, (3) Ostwald ripening. In cast iron, particle growth by collision can be excluded in the absence of adequate melt stirring because of a low collision probability of inclusions while ascending in the molten iron within the regime of Stoke's law. In addition, the diffusion-controlled desulfurization and deoxidation reactions (which involve diffusion of reactants in the melt to the sulfide and oxide nuclei) would be expected to be essentially complete within a few seconds when the number of particles is of the order of 10^5 per mm^3 or higher.[64] This implies that the observed increase in the inclusion diameter with time can solely be attributed to Ostwald ripening effects.

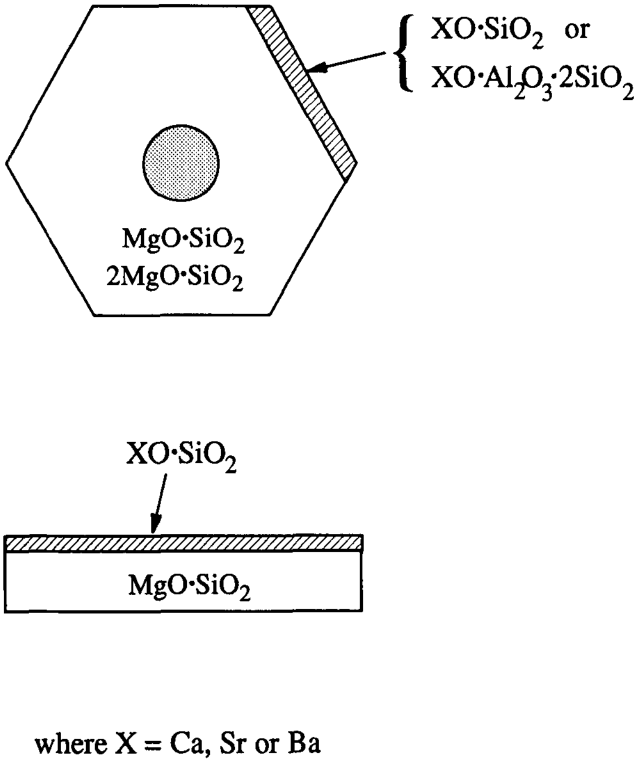

Fig. 15—Changes in the surface chemistry of type A and B inclusions after inoculation (schematic).

Broadly speaking, inclusion coarsening due to Ostwald ripening is a diffusion-controlled process where large particles grow at the expense of small ones. The driving force is provided by the reduction of the total particle/liquid interfacial area which, in turn, reduces the total free energy of the system. At steady state, the time dependence of the mean particle diameter (d) is given by the Wagner equation:[65]

$$d^3 = d_0^3 + \frac{64\sigma DCV_N^2}{9\,RT}\,t \qquad [30]$$

where d_0 is the initial particle diameter, σ is the particle-melt interfacial energy, D is the element diffusivity, C is the element bulk concentration, V_N is the molar volume of the inclusion phase per mole of the diffusate, and t is the holding time.

Taking d_0 equal to the average inclusion diameter in quenched samples (*i.e.*, 1.1 μm), Eq. [30] can be rewritten as

$$d_v\,(\mu m) = [1.33 + kt]^{1/3} \qquad [31]$$

where k is a parameter which is characteristic of the system under consideration (in the following assumed constant and independent of temperature).

In the present experiments, the time interval between inoculation and solidification of the 30-mm section size materials is of the order of 7 minutes. This means that the kinetic constant in Eq. [31] is close to 0.64 under the prevailing circumstances, taking $d_v = 1.8$ μm as a reasonable average value for such castings. Hence, Eq. [31] reduces to

$$d_v\,(\mu m) = [1.33 + 0.64t]^{1/3} \qquad [32]$$

where t is the holding time in minutes (referred to the time of addition of the inoculant).

Since the volume fraction of inclusions remains constant during the coarsening process due to a low flotation rate of the ascending particles, the total number of inclusions per unit volume (N_v) is inter-related to the mean inclusion diameter (d_v) through Eq. [27]. Combining Eqs. [27] and [32] gives

$$N_v\,(\text{no./mm}^3) = \frac{6V_v}{\pi(1.33 + 0.64t)} \times 10^9 \qquad [33]$$

Under isothermal conditions, Eq. [33] predicts that N_v is inversely proportional to the holding time t. Hence, after 20 minutes, the total number of inclusions per unit volume is reduced to about 10 pct of the initial value. Figure 16(a) shows a plot of the calculated number density of the inclusions in casting no. 3 as a function of the holding time t. The predicted shape of the N_v-t curve in Figure 16(a) is in close agreement with experimental observations (Figure 16(b)).

B. *Conditions for Graphite Formation*

1. *As-cast microstructures*

Data for the volume fraction of graphite, ferrite, pearlite, and iron carbide in the experimental castings are

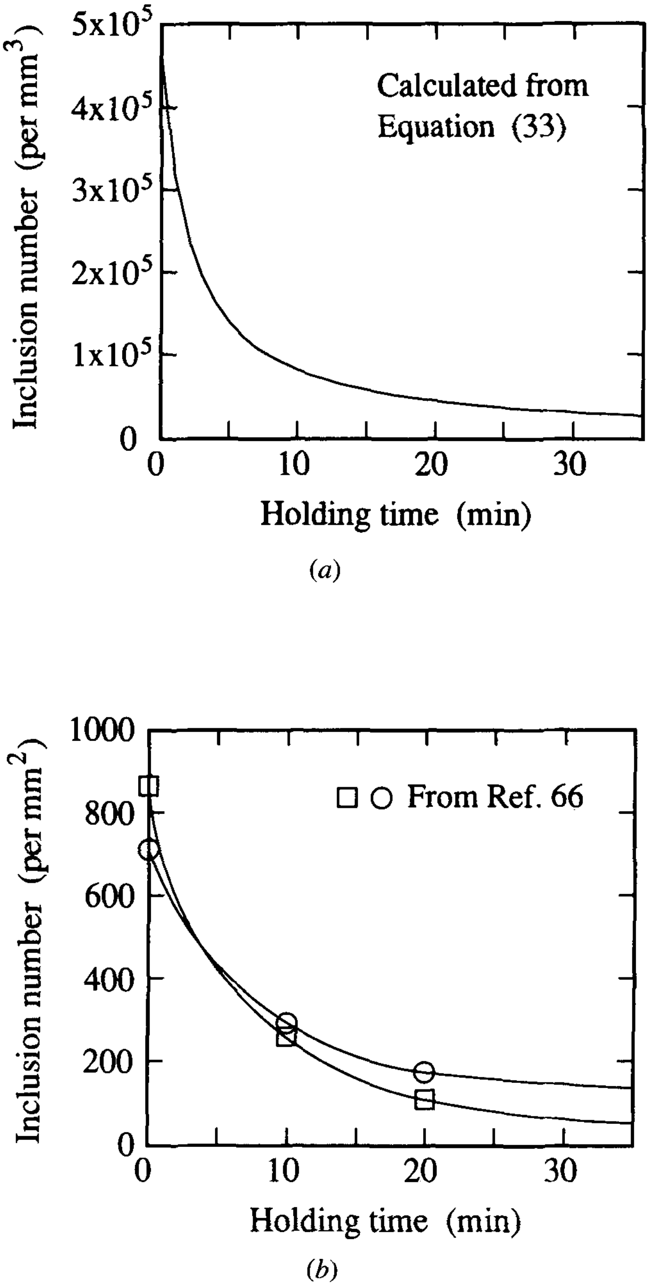

(*a*)

(*b*)

Fig. 16—Coarsening behavior of inclusions in ductile cast iron (*a*) calculated from Eq. [33] and (*b*) observed from measurements.[66]

Table XV. Microstructural Data for As-Cast 5-mm Section Size Materials

Casting	Graphite (Vol Pct)	Ferrite (Vol Pct)	Pearlite (Vol Pct)	Carbide (Vol Pct)
No. 1	10	58	32	—
No. 2	11	58	31	—
No. 3	10	65	25	—
No. 4	9	68	23	—
No. 5	12	62	26	—
No. 6	9	67	24	—
No. 7	3	19	37	41
No. 8	5	9	54	32
No. 9	1	10	36	53
No. 10	8	41	46	5
No. 11	5	48	46	1
No. 12	8	49	36	7

Table XVI. Microstructural Data for As-Cast 30-mm Section Size Materials

Casting	Graphite (Vol Pct)	Ferrite (Vol Pct)	Pearlite (Vol Pct)	Carbide (Vol Pct)
No. 1	10	87	3	—
No. 2	13	83	4	—
No. 3	12	80	8	—
No. 4	10	89	1	—
No. 5	11	86	3	—
No. 6	8	90	2	—
No. 7	10	50	37	3
No. 8	11	73	16	—
No. 9	9	40	43	8
No. 10	9	70	21	—
No. 11	10	86	4	—
No. 12	9	77	14	—

given in Tables XV and XVI. Examples of microstructures are presented in Figures 17 through 19.

In casting nos. 1 through 3, which are inoculated with (Ca,Al)-, (Sr,Al)-, and (Ca,Ba,Al)-containing ferrosilicon, respectively, the as-cast microstructures consist of graphite nodules embedded in a matrix of ferrite and pearlite (Figure 17). This type of microstructure is also found in casting nos. 4 through 6, which are nodularized with different Ca-Mg treatment alloys and inoculated with (Sr,Al)-containing ferrosilicon.

In cases where the inoculation treatment is omitted, a completely different microstructure is obtained. Referring to Figures 18(a) and (b), the dominating microconstituents in casting nos. 7 and 8 are pearlite and iron carbide. The same type of microstructure is also observed after inoculation with pure ferrosilicon (see micrographs of casting no. 9 in Figures 18(e) and (f)), which shows that the minor elements Ca, Sr, Ba, and Al play an important role in the graphite nodule evolution. However, it is evident from Figure 19 that casting nos. 10 through 12, which are inoculated with pure Al-, Ca-, and Sr-containing ferrosilicon, respectively, generally contain lower fractions of graphite than those produced by addition of complex inoculants to the melt (casting nos. 1 through 3). This suggests that the inoculation effect of Ca, Sr, and Ba is enhanced in the presence of aluminum.

2. *Nodule distribution*

Key results from the 2-D and 3-D graphite nodule size distribution measurements are summarized in Tables XVII and XVIII. Examples of measured nodule histograms are contained in Figures 20 and 21.

As expected, these data reveal a pattern which is in close agreement with that observed previously from the point-counting measurements. In general, high nodule densities are obtained in casting nos. 1 through 3, which are inoculated with (Ca,Al)-, (Sr,Al)-, and (Ca,Ba,Al)-containing ferrosilicon, respectively. The nodule densities are also high and relatively constant in casting nos. 4 through 6, which have been nodularized with different Ca-Mg treatment alloys and inoculated with (Sr,Al)-containing ferrosilicon. This shows that additions of calcium up to 2 wt pct through the magnesium-ferrosilicon treatment alloy do not significantly alter the

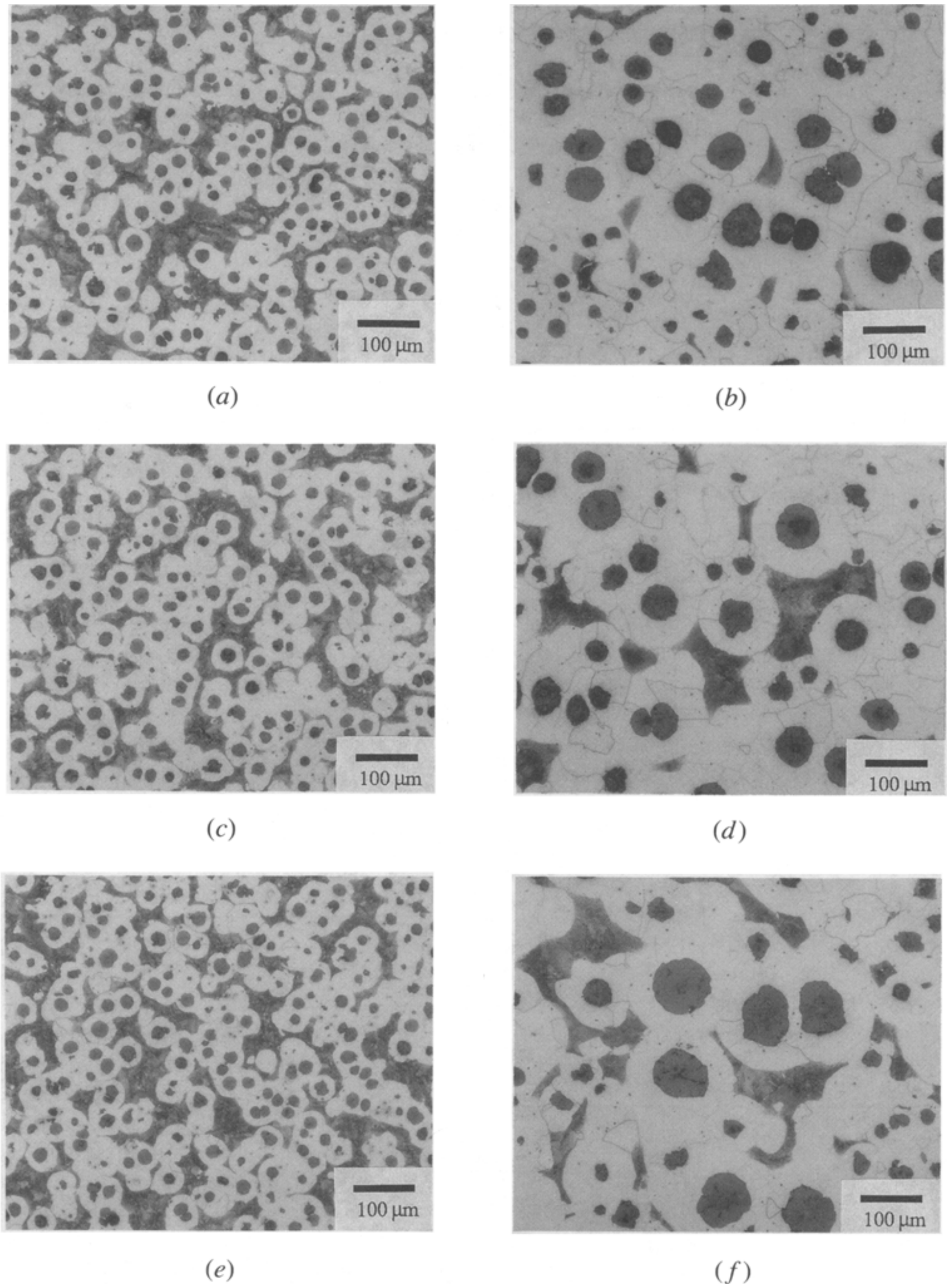

Fig. 17—Examples of microstructures in as-cast materials. Casting no. 1: (*a*) 5-mm and (*b*) 30-mm section size. Casting no. 2: (*c*) 5-mm and (*d*) 30-mm section size. Casting no. 3: (*e*) 5-mm and (*f*) 30-mm section size.

conditions for graphite nucleation under the prevailing circumstances.

On the other hand, the measured nodule densities in the noninoculated castings, nos. 7 and 8, are considerably lower than those observed in the previous castings. Moreover, an internal ranking of the two castings shows that the highest nodule density is achieved for the calcium-containing material (no. 8). This suggests that additions of calcium through the nodularizers can contribute to enhanced graphite nucleation in cases where the inoculation treatment is omitted. Also, casting no. 9, which is inoculated with pure ferrosilicon, reveals a very low nodule density. The latter observation confirms previous findings that pure silicon and ferrosilicon alloys are ineffective as inoculants in ductile cast iron (Section II–B).

Reasonable high nodule densities are also obtained in casting nos. 10 through 12, which are inoculated with Al-, Ca-, and Sr-containing ferrosilicon, respectively. However, the measured nodule densities are considerably lower than those achieved after inoculation with (Ca,Al)-, (Sr,Al)-, or (Ca,Ba,Al)-containing ferrosilicon alloys (casting nos. 1 through 6). This observation is not surprising, considering the fact that additions of Ca, Sr, or Ba along with Al make the former elements stronger inoculants than any of them alone.

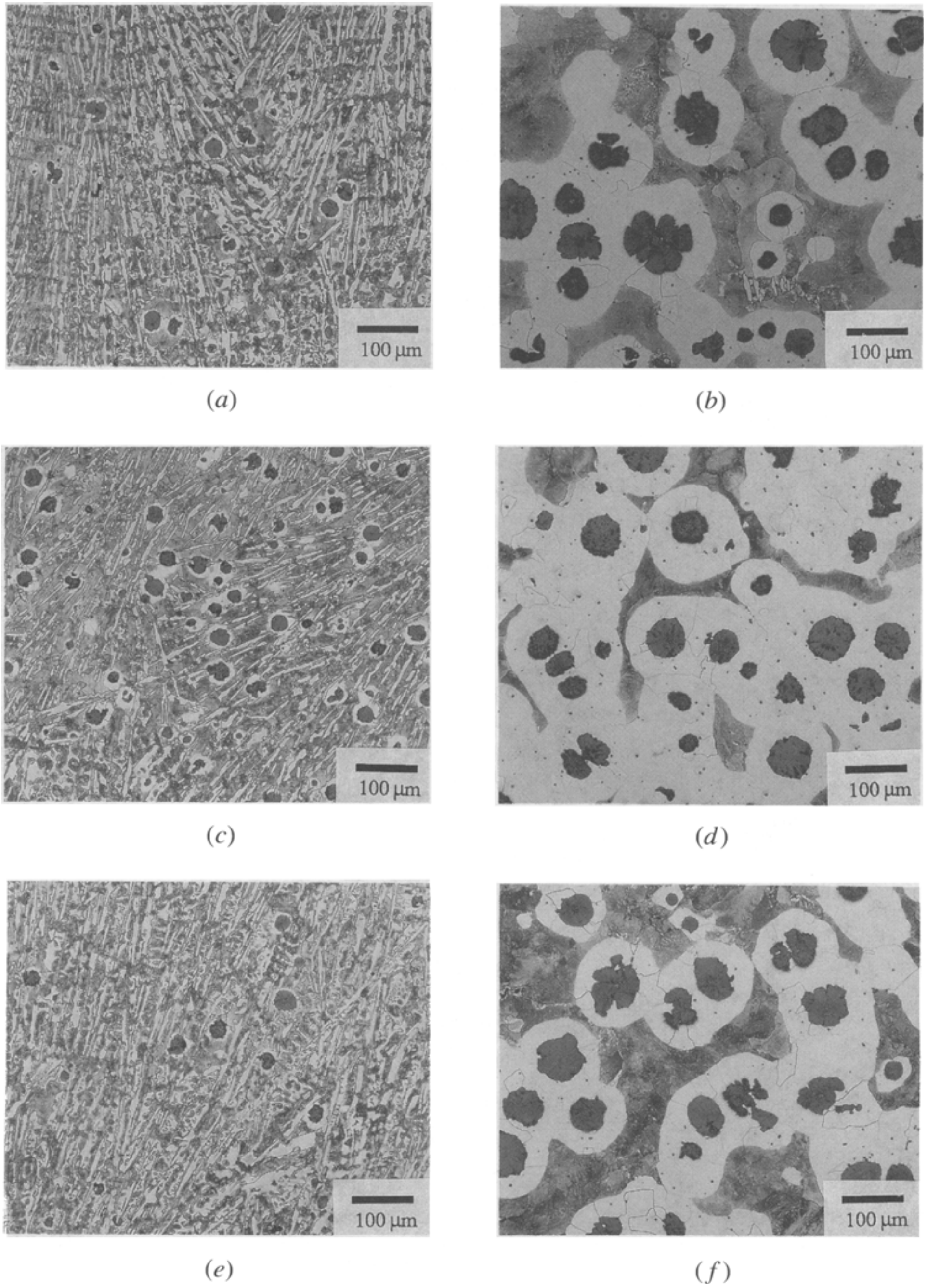

Fig. 18—Examples of microstructures in as-cast materials. Casting no. 7: (*a*) 5-mm and (*b*) 30-mm section size. Casting no. 8: (*c*) 5-mm and (*d*) 30-mm section size. Casting no. 9: (*e*) 5-mm and (*f*) 30-mm section size.

3. *Nature of catalyst particles*

Referring to Section II–B, there seems to be general agreement that nucleation of graphite in ductile cast iron occurs heterogeneously from particles contained in the melt. The problem has mainly been to determine the nature of these heterogenities, *i.e.*, their origin, composition, surface characteristics, stability, *etc.* It is evident from the SEM micrographs in Figure 22 that the graphite nucleation is preferentially associated with type A inclusions which consist of a sulfide core of MgS and CaS and an outer shell of $MgO \cdot SiO_2$ and $2MgO \cdot SiO_2$. Occasionally, type B inclusions ($MgO \cdot SiO_2$) are also observed in the center of graphite nodules.[48] It should be noted that the presence of these phases, in practice, is not a sufficient criterion for graphite formation, since a modification of the inclusion surface chemistry by additions of minor elements through the inoculants is always required to achieve a high nodule density. Consequently, the key to a better understanding of the microstructural evolution in ductile cast iron lies primarily in the recognition of the important difference between nodularization (magnesium treatment) and inoculation with regard to graphite nucleation.

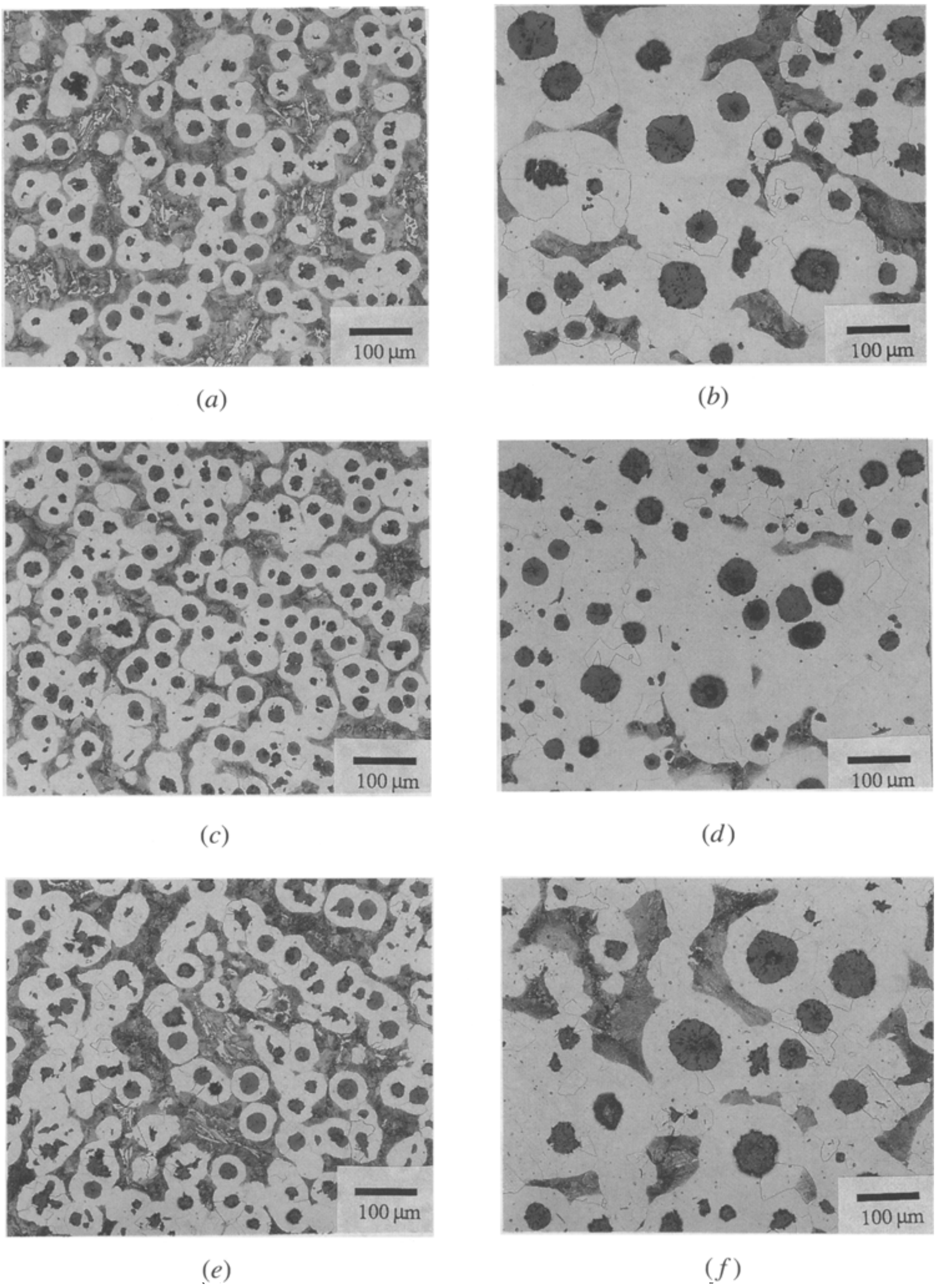

(*a*) (*b*)

(*c*) (*d*)

(*e*) (*f*)

Fig. 19—Examples of microstructures in as-cast materials. Casting no. 10: (*a*) 5-mm and (*b*) 30-mm section size. Casting no. 11: (*c*) 5-mm and (*d*) 30-mm section size. Casting no. 12: (*e*) 5-mm and (*f*) 30-mm section size.

4. *Bramfitt's Planar Lattice Disregistry Model*

As already stated in Section I, the interfacial energy at the nucleating interface (γ_{GN}) is the controlling factor in heterogeneous nucleation. For fully incoherent interfaces, γ_{GN} would be expected to be of the order of 0.5 to 1 J/m^2.[3] However, this value will be greatly reduced if there is epitaxy between the inclusions and the graphite nucleus, which results in a low lattice disregistry between the two phases. In general, assessment of the degree of atomic misfit between the graphite (G) and the nucleant (N) can be done on the basis of the Bramfitt's planar lattice disregistry model:[4]

$$\delta = \sum_{i=1}^{3} \frac{1}{3} \left(\frac{|(d_{[uvw]_N^i} \cos \alpha) - d_{[uvw]_G^i}|}{d_{[uvw]_N^i}} \right) \times 100 \text{ pct} \qquad [34]$$

where

$[uvw]_N$ = a low-index direction in $(hkl)_N$;
$[uvw]_G$ = a low-index direction in $(hkl)_G$;
$d_{[uvw]_N}$ = the interatomic spacing along $[uvw]_N$;
$d_{[uvw]_G}$ = the interatomic spacing along $[uvw]_G$; and
α = the angle between the $[uvw]_N$ and the $[uvw]_G$.

Table XVII. Graphite Nodule Characteristics for As-Cast 5-mm Section Size Materials

Casting	D_V (μm)	N_A (mm^{-2})	N_V (mm^{-3})
No. 1	14.6	349	27,188
No. 2	20.6	352	18,169
No. 3	23.3	350	17,152
No. 4	20.0	359	19,325
No. 5	17.2	402	25,970
No. 6	19.0	394	22,595
No. 7	17.8	56	3433
No. 8	24.2	151	6769
No. 9	18.2	52	3102
No. 10	26.4	228	9077
No. 11	23.8	276	12,207
No. 12	25.2	219	9223

Table XVIII. Graphite Nodule Characteristics for As-Cast 30-mm Section Size Materials

Casting	D_V (μm)	N_A (mm^{-2})	N_V (mm^{-3})
No. 1	22.2	153	7429
No. 2	26.1	133	5278
No. 3	35.8	126	3736
No. 4	24.6	176	7553
No. 5	22.9	178	8141
No. 6	26.2	160	6416
No. 7	37.2	48	1343
No. 8	42.6	75	1788
No. 9	33.1	54	1711
No. 10	40.4	86	2190
No. 11	25.3	251	10,663
No. 12	45.6	82	1847

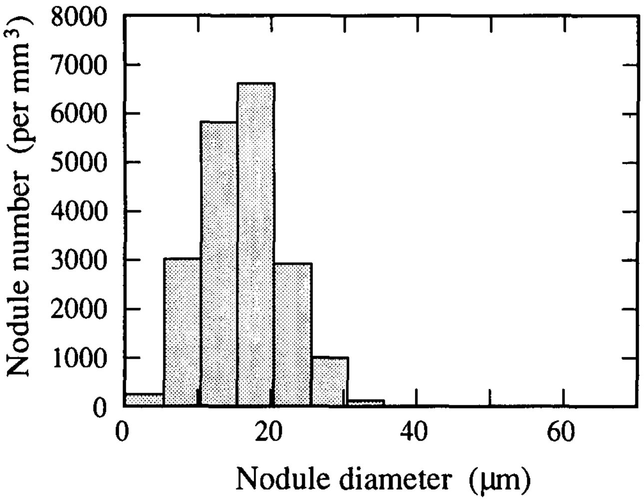

Fig. 20—3-D size distribution of graphite nodules in casting no. 2 (5-mm section size material).

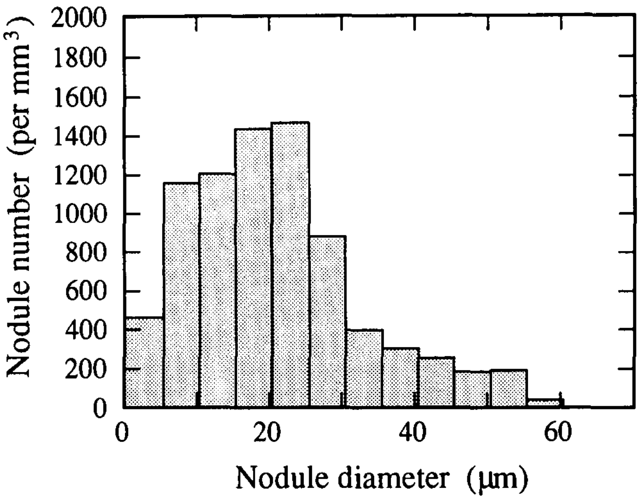

Fig. 21—3-D size distribution of graphite nodules in casting no. 2 (30-mm section size material).

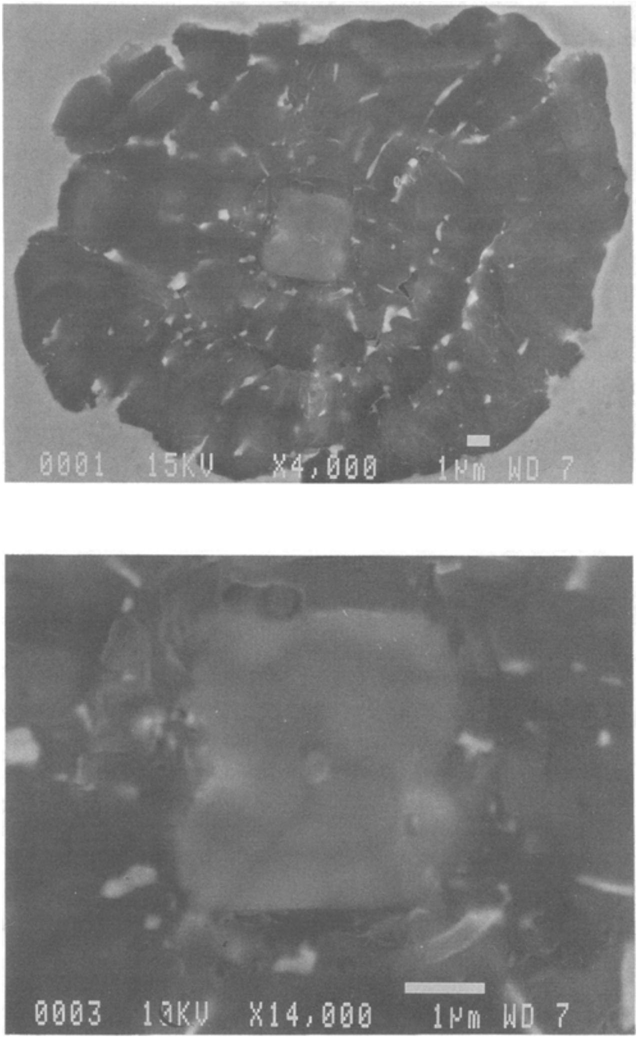

Fig. 22—SEM micrographs showing evidence of graphite nucleation at type A inclusion in casting no. 11.

In practice, the undercooling ΔT (which is a measure of the energy barrier against heterogeneous nucleation) increases monotonically with increasing values of the planar lattice disregistry δ, as shown in Figure 2. This means that the most potent catalyst particles are those which provide a good epitaxial fit between the nucleant and the graphite embryo.

5. *Nucleation of graphite at inclusions*

The characteristic irregular shape of the type A and B inclusions indicates a faceted growth morphology. Faceted growth occurs as a result of anisotropy in the growth rates between high-index and low-index crystallographic planes.[67] If the former type of planes are the fastest growing ones, these planes will soon grow out, leaving a faceted crystal delimited solely by low-index planes.

a. *$MgO \cdot SiO_2$ and $2MgO \cdot SiO_2$*

The probable crystal growth morphologies of enstatite ($MgO \cdot SiO_2$) and forsterite ($2MgO \cdot SiO_2$) are shown in Figure 23. Included in the figure is also a sketch of the lattice arrangement at the interface between the (100) plane of $MgO \cdot SiO_2$ and the (001) plane of graphite. This orientation relationship conforms to growth of the graphite along the pole of the basal plane perpendicular to the inclusion surface, which is the normal growth mode of graphite in ductile cast iron.[55] By only considering the position of the corner atoms in the orthorhombic unit cell (Figure 23(c)), the planar lattice disregistry between graphite, enstatite, and forsterite has been calculated from Eq. [34] for a wide spectrum of orientation relationships. The results from these computations are summarized in Table XIX.

It is evident from the data in Table XIX that the chances of obtaining a small planar lattice disregistry between graphite, $MgO \cdot SiO_2$, or $2MgO \cdot SiO_2$ are rather poor, which means that the energy barrier against heterogeneous nucleation is correspondingly high. Hence, these phases, which are primary products of the magnesium treatment, would not be expected to act as favorable nucleation sites for graphite during solidification, in agreement with general experience.

b. *$XO \cdot SiO_2$ and $XO \cdot Al_2O_3 \cdot 2SiO_2$*

Referring to Figure 24, phases of the $XO \cdot SiO_2$ and the $XO \cdot Al_2O_3 \cdot 2SiO_2$ type also tend to form faceted crystals because of anisotropy in the growth rate between high-index and low-index crystallographic planes. In particular, the (001) basal planes of the crystals will be favorable sites for graphite nucleation, since these facets allow for formation of coherent/semicoherent low-energy interfaces between the nucleant and the graphite, as illustrated in Figure 25. In fact, nearly all of the hexagonal silicate phases of the $XO \cdot SiO_2$ and $XO \cdot Al_2O_3 \cdot 2SiO_2$ type which form at the surface of the inclusions after the inoculation treatment are effective catalyst particles for graphite (Table XX). This explains why commercial inoculants for cast iron are based on calcium, strontium, or barium.

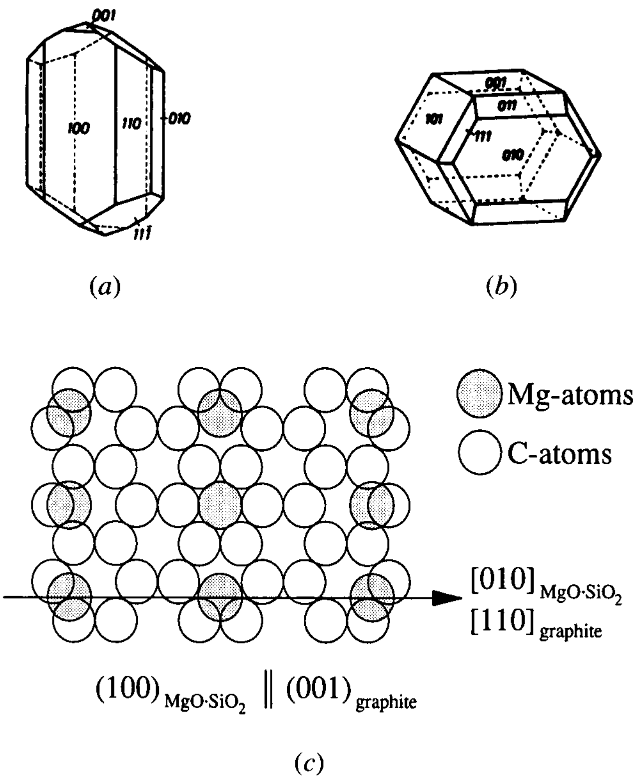

(*a*) (*b*)

(*c*)

Fig. 23—Nucleation of graphite at enstatite ($MgO \cdot SiO_2$) and forsterite ($2MgO \cdot SiO_2$): (*a*) crystal form of $MgO \cdot SiO_2$;[63] (*b*) crystal form of $2MgO \cdot SiO_2$;[63] and (*c*) details of lattice arrangement at graphite/$MgO \cdot SiO_2$ interface (schematic).

Table XIX. Calculated Planar Lattice Disregistry between Enstatite, Forsterite, and Graphite for Different Orientation Relationships

Inclusion Phase	Orientation Relationship*	Lattice Disregistry
Enstatite $MgO \cdot SiO_2$	$(100)_I \parallel (001)_G$	10.2 pct
	$(010)_I \parallel (001)_G$	8.7 pct
	$(001)_I \parallel (001)_G$	5.9 pct
	$(110)_I \parallel (001)_G$	12.3 pct
	$(111)_I \parallel (001)_G$	10.1 pct
Forsterite $2MgO \cdot SiO_2$	$(100)_I \parallel (001)_G$	9.9 pct
	$(010)_I \parallel (001)_G$	24.3 pct
	$(001)_I \parallel (001)_G$	15.5 pct
	$(101)_I \parallel (001)_G$	25.5 pct
	$(111)_I \parallel (001)_G$	29.7 pct

*I = inclusion and G = graphite.

It follows from Table XX that even pure corundum (α-Al_2O_3) may assist the graphite nucleation in ductile cast iron due to a small lattice disregistry between the (001) plane of α-Al_2O_3 and the (001) plane of graphite. Although corundum is not a common reaction product in cast iron, it can probably form in cases where the melt contains remnants of dissolved oxygen, according to the equation

$$2\underline{Al} + 3\underline{O} = Al_2O_3 \qquad [35]$$

Formation of small amounts of corundum at the surface of the inclusions may explain why pure aluminum-containing ferrosilicon is seen to have a weak inoculating effect in ductile cast iron, as shown previously by the microstructural data in Tables XV through XVIII.

6. *Rate of graphite nucleation*

As shown in Section II–A, the rate of graphite nucleation in ductile cast iron can be expressed as

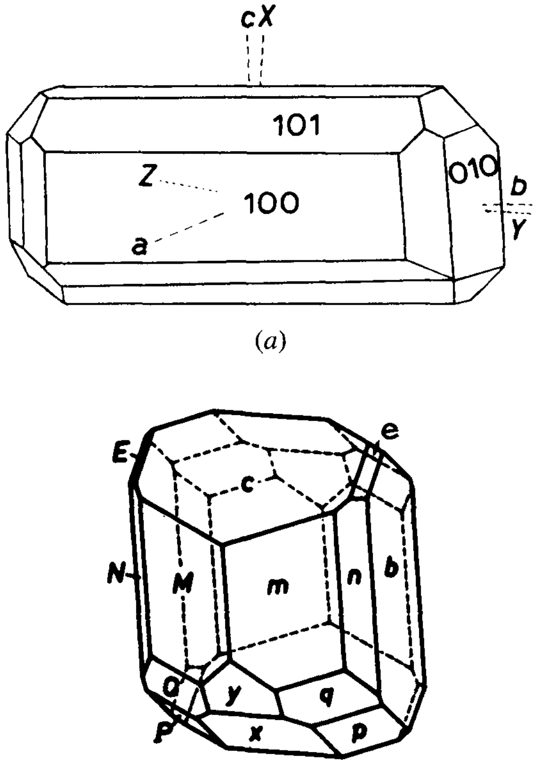

(a)

(b)

Fig. 24—Crystal forms of wollastonite ($CaO{\cdot}SiO_2$) and anorthite ($CaO{\cdot}Al_2O_3{\cdot}2SiO_2$):[63] (a) $CaO{\cdot}SiO_2$ and (b) $CaO{\cdot}Al_2O_3{\cdot}2SiO_2$.

$$\dot{N} \approx \nu N_V \exp\left(-\frac{\Delta G^*}{kT}\right) \qquad [36]$$

when $\Delta G_D \ll \Delta G^*$.

Provided that $\dot{N}$ is constant (*i.e.*, inclusion coarsening can be neglected), the total number of graphite nodules which form during solidification, N_V (gr), is given by

$$N_V = \dot{N}\Delta t_S = \nu \Delta t_S N_V\,(\text{incl}) \exp\left(-\frac{\Delta G^*}{kT}\right) \qquad [37]$$

where Δt_S is the total solidification time and N_V (incl) denotes the total number of inclusions per unit volume of the melt.

In the limiting case where the product ($\nu\Delta t_S$) is equal to unity, Eq. [37] reduces to

$$N_V\,(\text{gr}) = N_V\,(\text{incl}) \exp\left(-\frac{\Delta G^*}{kT}\right) \qquad [38]$$

It is seen from the graphical representation of Eq. [38] in Figure 26 that the N_V (gr) to N_V (incl) ratio is sensitive to variations in the energy barrier ΔG^*. Based on the inclusion and graphite nodule data in Tables XIII and XVIII, respectively, it can be argued that this ratio typically varies from 0.03 to 0.1 for inoculated castings and from 0.006 to 0.01 for noninoculated castings. Although the preceding values are encumbered by considerable uncertainty, the observed range in the N_V (gr) to N_V (incl) ratio conforms to a span in normalized energy barrier $\Delta G^*/kT$ from 2.3 to 5.1, as indicated in Figure 26. Such variations in ΔG^* are not surprising, considering the pertinent difference in the undercooling between inoculated and noninoculated castings (typically 2 °C to 8 °C and 10 °C to 20 °C, respectively).

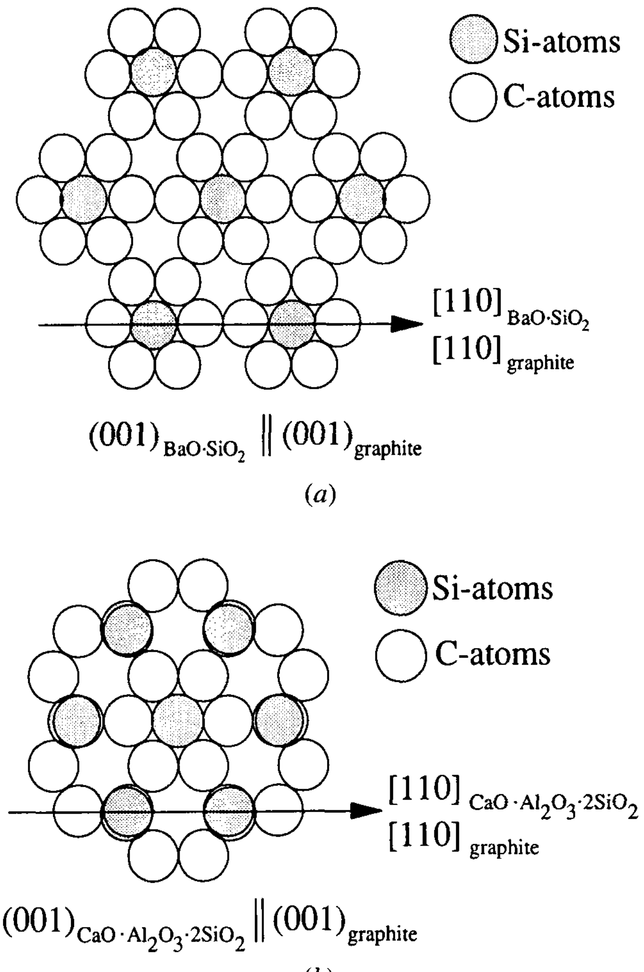

(a)

(b)

Fig. 25—Details of lattice arrangement at nucleus/substrate interface: (a) coherent graphite/$BaO{\cdot}SiO_2$ interface and (b) coherent graphite/$CaO{\cdot}Al_2O_3{\cdot}2SiO_2$ interface.

Table XX. Calculated Planar Lattice Disregistry between Graphite and Different Inclusion Constituent Phases which Form during Inoculation

Inclusion Phase	Orientation Relationship*	Lattice Disregistry
$CaO{\cdot}SiO_2$	$(001)_I \parallel (001)_G$	7.5 pct
$SrO{\cdot}SiO_2$	$(001)_I \parallel (001)_G$	3.5 pct
$BaO{\cdot}SiO_2$	$(001)_I \parallel (001)_G$	1.5 pct
$CaO{\cdot}Al_2O_3{\cdot}2SiO_2$	$(001)_I \parallel (001)_G$	3.7 pct
$SrO{\cdot}Al_2O_3{\cdot}2SiO_2$	$(001)_I \parallel (001)_G$	6.2 pct
$BaO{\cdot}Al_2O_3{\cdot}2SiO_2$	$(001)_I \parallel (001)_G$	7.1 pct
α-Al_2O_3	$(001)_I \parallel (001)_G$	3.4 pct

*I = inclusion and G = graphite.

7. *Fading of inoculation*

So far, a verified quantitative understanding of the fading mechanism in ductile cast iron is lacking. However, in view of the results obtained in Section IV–A–7, it is reasonable to assume that the phenomenon is related to a general coarsening of the inclusion population with time, which reduces the total number of possible nucleation sites for graphite. Following that treatment, the total number of inclusions per cubic millimeter of the melt is given by Eq. [33]. By substituting Eq. [33] into Eq. [36], it is possible to obtain a simple expression for the nucleation rate of the graphite nodules:

$$\frac{dN_V(\mathrm{gr})}{dt} = \nu \frac{6V_V \times 10^9}{\pi(1.33 + 0.64t)} \exp\left(-\frac{\Delta G^*}{kT}\right) \qquad [39]$$

Provided that the parameters ν, V_V, and $\Delta G^*/kT$ remain constant during the solidification process, integration of Eq. [39] between the limits t_S and t_E gives

$$N_V(\mathrm{gr}) = c[\ln(1.33 + 0.64t_E) - \ln(1.33 + 0.64t_S)] \qquad [40]$$

where c is an unknown kinetic constant and t_S and t_E are the time intervals between inoculation and start and end of solidification, respectively.

The time interval t_E can alternatively be expressed as

$$t_E = t_S + \Delta t_S \qquad [41]$$

where Δt_S is the total solidification time (in minutes). This gives

$$N_V(\mathrm{gr}) = c[\ln(1.33 + 0.64(t_S + \Delta t_S)) - \ln(1.33 + 0.64t_S)] \qquad [42]$$

For a given casting, the maximum graphite nodule density, $N_V^M(\mathrm{gr})$, is defined by $t_S = 0$. In other cases ($t_S > 0$), the nodule density will be lower than $N_V^M(\mathrm{gr})$, since particle coarsening will tend to reduce the total number of nucleation sites for graphite during solidification. The unknown kinetic constant in Eq. [42] can, in turn, be eliminated by introducing the relative nodule density (RND), defined as

$$\mathrm{RND(pct)} = \frac{N_V(\mathrm{gr})}{N_V^M(\mathrm{gr})} \times 100 = \frac{\ln[1.33 + 0.64(t_S + \Delta t_S)] - \ln[1.33 + 0.64t_S]}{\ln[1.33 + 0.64\Delta t_S] - \ln[1.33]} \times 100 \qquad [43]$$

It follows from the graphical representation of Eq. [43] in Figure 27(a) that the percental reduction in the graphite nodule density with increasing holding time will be most pronounced in thin section materials (characterized by a short solidification time), since the coarsening rate of the inclusions is highest during the initial stage of the process. Although fading curves for ductile cast iron are normally based on real nodule counts, a comparison with the normalized literature data in Figure 27(b) shows a very good agreement between theory and experiments in all cases, which confirms that the model is sound. Since the fading mechanism in ductile cast iron is clearly related to a general coarsening of the inclusion population

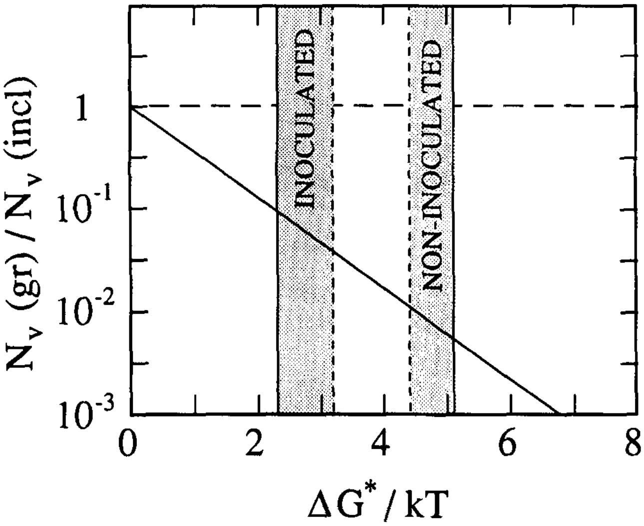

Fig. 26—Graphical representation of Eq. [38].

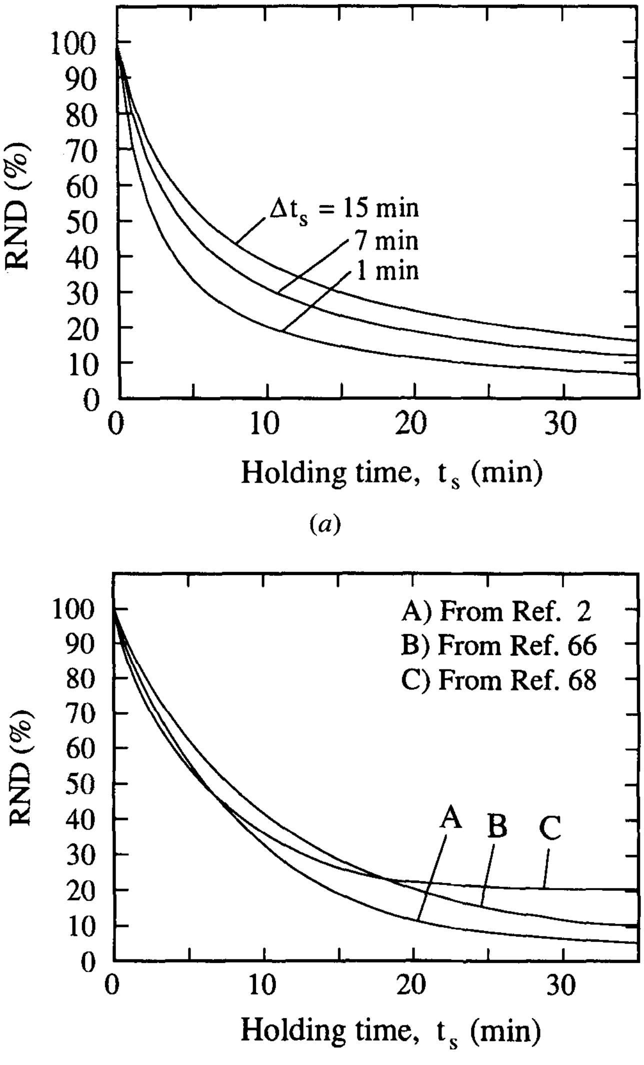

Fig. 27—Fading curves for ductile cast iron (*a*) calculated from Eq. [43] and (*b*) observed from measurements (Ca- and Sr-containing inoculants).

with time, reinoculation of the melt after an initial period of isothermal holding would not be expected to significantly alter the conditions for graphite formation during solidification unless the melt contains remnants of free oxygen. This is also in agreement with practical experience.[69]

V. PRACTICAL IMPLICATIONS

The proposed model for the graphite formation in ductile cast iron can explain several of the well-known phenomena observed in connection with nodularization and inoculation of such materials.

Today, the majority of the commercial inoculants and Mg-treatment alloys are based on ferrosilicon, and experience shows that silicon plays an important role in the development of the nodular graphite microstructure. Besides being a carrier for the minor elements, silicon will also enter the deoxidation products during nodularization, which facilitates the formation of the catalyst silicate phases at the surface of the inclusions during the subsequent inoculation stage.

Moreover, it is well established that minor additions of aluminum to calcium-containing ferrosilicon will increase the graphite nucleation capacity of the inoculant, although successful inoculation also can be achieved without aluminum additions. This observation is probably related to formation of anorthite ($CaO \cdot Al_2O_3 \cdot 2SiO_2$) at the surface of the inclusions, which is an important catalyst phase for graphite in ductile cast iron (Table XX). The situation is slightly different in the case of strontium-containing inoculants. Here, aluminum in high concentrations will promote the chilling susceptibility of the castings.[11] This phenomenon can probably be attributed to a relatively large lattice disregistry between graphite and $SrO \cdot Al_2O_3 \cdot 2SiO_2$ compared with pure $SrO \cdot SiO_2$ (6.1 pct *vs* 3.5 pct) which is the stable phase at low Al levels.

Moreover, based on the results obtained in the present investigation, it is also possible to explain why the graphite nodule density in ductile cast iron often is seen to pass through a local maximum with increasing contents of Ca, Sr, or Ba in the inoculants. Figure 28(a) shows an example of the effect of calcium additions on the graphite formation in ductile cast iron. It is evident from these literature data that a Ca content beyond approximately 0.8 wt pct in the ferrosilicon alloy will have a clear negative influence on the nodule count under the prevailing circumstances. This situation arises probably from a change in the chemical composition of the reaction products from enstatite ($CaO \cdot SiO_2$) and anorthite ($CaO \cdot Al_2O_3 \cdot 2SiO_2$) at low and medium Ca levels to rankinite ($3CaO \cdot 2SiO_2$) or grossularite ($3CaO \cdot Al_2O_3 \cdot 3SiO_2$) at higher Ca levels, as indicated in Figure 28(b). The latter phases do not allow for a good epitaxial fit between the substrate and the graphite nucleus and will therefore suppress the graphite formation in ductile cast iron.

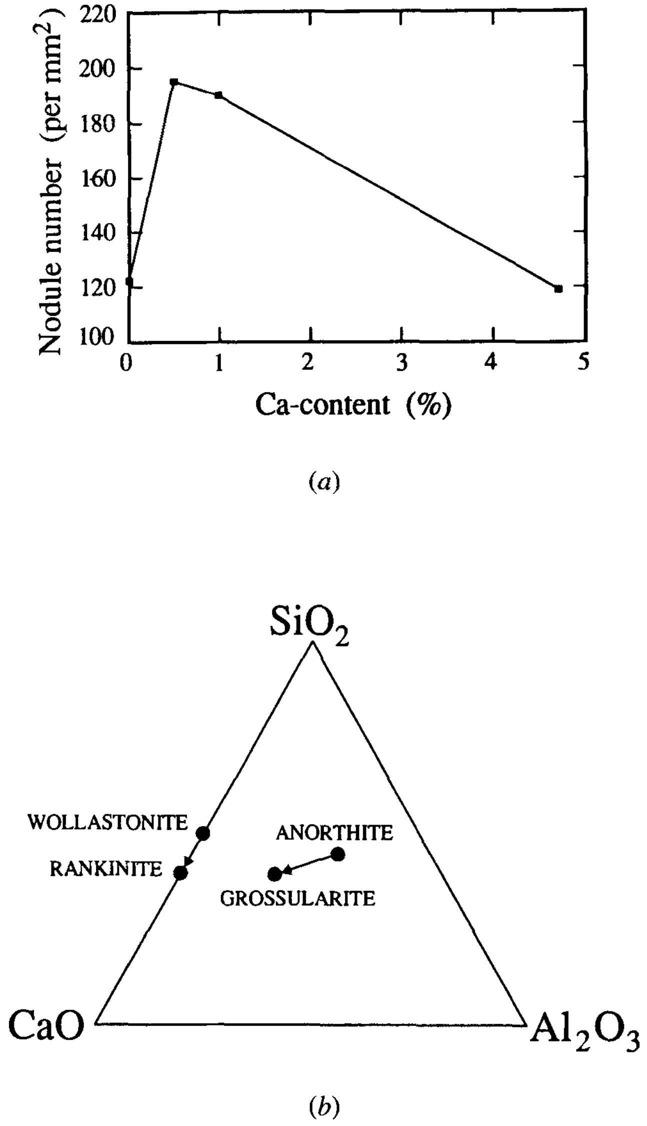

Fig. 28—Effects of calcium in ductile cast iron: (*a*) nodule count *vs* Ca content in inoculant[70] and (*b*) possible phases in inclusions at low and high Ca levels.

Finally, the present model explains why, for instance, calcium additions through the magnesium-ferrosilicon treatment alloy do not result in the formation of the same favorable hexagonal silicate phases as those observed at the surface of the inclusions after inoculation. When calcium is added together with magnesium in ratios up to 7:3, the stoichiometric phase diopside ($CaO \cdot MgO \cdot 2SiO_2$) will form.[63] This phase is very stable and has a monocline crystal structure which does not match the graphite lattice. Hence, successive magnesium treatment and inoculation are always required to achieve a high graphite nodule density in ductile cast iron.

VI. CONCLUSIONS

The basic conclusions that can be drawn from this investigation are the following.

1. In magnesium-treated cast irons, the inclusions can be divided into three main categories:

   type A inclusions, which contain Mg, Ca, S, and Si;

   type B inclusions, which contain Mg and Si; and type C inclusions, which contain Mg, P, and REM (*e.g.*, Ce and La).

The type A and B inclusions are primary reaction products of the magnesium treatment, while the latter group stems from reactions between dissolved magnesium and phosphorus during solidification.

2. The type A inclusions are composed of a sulfide core and a faceted outer silicate shell. The sulfide core contains both MgS and CaS, while the outer shell consists of complex magnesium silicates (*e.g.*, $MgO\cdot SiO_2$ and $2MgO\cdot SiO_2$). In contrast, the type B inclusions are probably single-phase particles of enstatite ($MgO\cdot SiO_2$) which precipitates homogeneously in the melt during nodularization. These phases will not act as potent nucleation sites for graphite during solidification because of a large planar lattice disregistry between the graphite nucleus and the substrate.
3. After inoculation with an (X,Al)-containing ferrosilicon (X denotes Ca, Sr, or Ba), hexagonal silicate phases of the $XO\cdot SiO_2$ or the $XO\cdot Al_2O_3\cdot 2SiO_2$ type can form at the surface of the oxide inclusions. This occurs most probably through an exchange reaction with MgO. In particular, the (001) basal planes of the crystals will be favorable sites for graphite nucleation, since these facets allow for the formation of coherent/semicoherent low-energy interfaces between the nucleant and the graphite.
4. In ductile cast iron, the fading of inoculation can be explained by a general coarsening of the inclusion population with time, which reduces the total number of possible nucleation sites for graphite during solidification. A theoretical analysis of the reaction kinetics gives results which are in close agreement with experimental observations.

ACKNOWLEDGMENTS

The authors acknowledge the financial support and technical assistance from Bjølvefossen a/s and Elkem a/s. In addition, the review and comments by Messrs. S.O. Olsen, J. Sandvik, and K. Jørgensen (Bjølvefossen) and B. Jensen (Elkem) are gratefully acknowledged.

REFERENCES

1. V.H. Patterson and M.J. Lalich: *AFS Trans.*, 1978, vol. 86, pp. 33-42.
2. R. Elliott: *Cast Iron Technology*, Butterworth's, London, 1988, pp. 79-85.
3. D.A. Porter and K.E. Easterling: *Phase Transformations in Metals and Alloys*, Van Nostrand Reinhold, Wokingham, United Kingdom, 1981, pp. 110-262.
4. Bruce L. Bramfitt: *Metall. Trans.*, 1970, vol. 1, pp. 1987-95.
5. L.F. Mondolfo: *Mater. Sci. Technol.*, 1989, vol. 5, pp. 118-22.
6. Y. Nuri, T. Ohashi, T. Hiromoto, and O. Kitamura: *Trans. Iron Steel Inst. Jpn.*, 1982, vol. 22, pp. 399-407.
7. T. Skaland, Ø. Grong, and T. Grong: *Metall. Trans. A*, 1993, vol. 24A, pp. 2347-53.
8. I. Minkoff: *The Physical Metallurgy of Cast Iron*, John Wiley & Sons Ltd., New York, NY, 1983, pp. 55-63.
9. D. Turnbull and R. Vonnegut: *Ind. Eng. Chem.*, 1952, vol. 44, pp. 1292-97.
10. I.C. Hughes: *Proc. Sol. Tech. in the Foundry and Casthouse*, Institute of Metals, London, 1980.
11. J.V. Dawson: *BCIRA J.*, 1961, vol. 9, pp. 199-236.
12. H.W. Lownie: *Foundry*, 1963, vol. 91, pp. 66-68.
13. J.V. Dawson: *Modern Casting*, 1966, vol. 49, pp. 171-77.
14. N.C. McClure, A.V. Khan, D. McCrady, and H.L. Womochel: *AFS Trans.*, 1957, vol. 65, pp. 340-49.
15. R.L. Nickelson: *Foundry*, 1967, vol. 95, pp. 145-49.
16. C.S. Kanetkar, H.H. Carnell, and D.M. Stefanescu: *AFS Trans.*, 1984, vol. 92, pp. 417-28.
17. A. Boyles: *The Structure of Cast Iron*, ASM, Metals Park, OH, 1947.
18. J.T. Eash: *AFS Trans.*, 1941, vol. 49, pp. 887-906.
19. G.A. Feest, G. McHugh, D.O. Morton, L.S. Welch, and I.A. Cook: *Proc. Sol. Tech. in the Foundry and Casthouse*, The Metals Society, London, 1983, pp. 232-39.
20. N. Kayama and K. Suzuki: *Report Casting Research Lab.*, Waseda University, Japan, 1979, vol. 30, pp. 61-67.
21. C.H. Wang and H. Fredriksson: *Proc. 48th Int. Foundry Congress*, 1981, Varna, Bulgaria.
22. H. Fredriksson: *Mater. Sci. Eng.*, 1984, vol. 65, pp. 137-44.
23. B. Lux: *Modern Casting*, 1964, vol. 45, pp. 222-32.
24. K.M. Muzumdar and J.F. Wallace: *AFS Trans.*, 1972, vol. 80, pp. 317-28.
25. M.H. Jacobs, T.J. Law, D.A. Melford, and M.J. Stowell: *Met. Technol.*, 1974, vol. 1, pp. 490-500.
26. M.A. Gadd and G.H.J. Bennett: *Physical Chemistry of Inoculation in Cast Iron*, 3rd Int. Symp. on the Physical Metallurgy of Cast Iron, Stockholm, 1984.
27. G.X. Sun and C.R. Loper, Jr.: *AFS Trans.*, 1983, vol. 91, pp. 639-46.
28. R. Naro and J.F. Wallace: *AFS Trans.*, 1970, vol. 78, pp. 229-38.
29. K. Muzumdar and J.F. Wallace: *AFS Trans.*, 1973, vol. 81, pp. 412-23.
30. M.J. Lalich and J.R. Hitchings: *AFS Trans.*, 1976, vol. 84, pp. 653-64.
31. A.P. Rosenstiel and H. Bakkerus: *Giesserei Tech. Wiss. Beih.*, 1964, vol. 16, pp. 149-54.
32. W. Deuchler: *Giesserei Tech. Wiss. Beih.*, 1962, vol. 14, pp. 745-51.
33. H.B. Zeedijk: *J. Iron Steel Inst.*, 1965, vol. 203, pp. 737-38.
34. B. Dhindaw and J.D. Verhoeven: *Metall. Trans. A*, 1980, vol. 11A, pp. 1049-57.
35. J.C. Mercier: *Fonderia*, 1969, No. 277, pp. 191-97.
36. M.H. Jacobs, T.J. Law, D.A. Melford, and M.J. Stowell: *Met. Technol.*, 1976, vol. 3, pp. 98-108.
37. R.J. Warrick: *AFS Cast Met. Res. J.*, 1966, vol. 2 (3), pp. 97-108.
38. D.R. Askeland, P.K. Trojan, and R.A. Flinn: *AFS Trans.*, 1970, vol. 78, pp. 125-32.
39. D.R. Askeland and P.K. Trojan: *AFS Trans.*, 1969, vol. 77, pp. 344-52.
40. B. Francis: *Metall. Trans. A*, 1979, vol. 10A, pp. 21-31.
41. R.W. Heine and C.R. Loper, Jr.: *AFS Trans.*, 1966, vol. 74, pp. 274-80.
42. D.R. Askeland, P.K. Trojan, and R.A. Flinn: *AFS Trans.*, 1972, vol. 80, pp. 349-58.
43. R.W. Heine and C.R. Loper, Jr.: *AFS Trans.*, 1966, vol. 74, pp. 421-28.
44. M.C. Latona, H.W. Kwon, J.F. Wallace, and J.D. Voss: *AFS Trans.*, 1984, vol. 92, pp. 881-906.
45. P.K. Trojan, P.J. Guichelaar, W.N. Bargeron, and R.A. Flinn: *AFS Trans.*, 1968, vol. 76, pp. 323-33.
46. A. Wittmoser: *Giesserei Tech. Wiss. Beih.*, 1952, No. 6–8, pp. 323-34.
47. I. Barin: *Thermochemical Data of the Pure Substances*, VCH Verlagsgesellschaft, Weinheim, Germany, 1989.
48. R. Kiessling and N. Lange: *Non-Metallic Inclusions in Steel*, Book No. 194, The Metals Society, London, 1978.
49. D.L. Sponseller and R.A. Flinn: *Trans. TMS-AIME*, 1964, No. 230, pp. 876-88.
50. R.H. Rein and J. Chipman: *Trans. TMS-AIME*, 1965, vol. 233, pp. 415-25.
51. J. Bruch: *Rheinstahl Technol.*, 1965, No. 2, pp. 211-22.
52. J. Bruch: *Rheinstahl Technol.*, 1965, No. 36, pp. 799-807.

53. J.R. Wynnyckyj and L.M. Pidgeon: *Metall. Trans.*, 1971, vol. 2, pp. 979-86.
54. J.P. Sadocha and J.E. Gruzleski: *Proc. 2nd Int. Symp. on the Metallurgy of Cast Iron*, Geneva, 1974, pp. 443-56.
55. R.H. McSwain and C.E. Bates: *Proc. 2nd Int. Symp. on the Metallurgy of Cast Iron*, Geneva, 1974, pp. 423-40.
56. I. Minkoff: *Proc. Solidification of Metals*, ISI, Philadelphia, PA, 1968, vol. P110, p. 253-65.
57. D.D. Double and A. Hellawell: *Proc. 2nd Int. Symposium on the Metallurgy of Cast Iron*, Geneva, 1974, pp. 509-25.
58. B. Lux, I. Minkoff, F. Mollard, and E. Thury: *Proc. 2nd Int. Symp. on the Metallurgy of Cast Iron*, Geneva, 1974, pp. 495-505.
59. E.E. Underwood: *Quantitative Stereology*, Addison-Wesley Publishing Co., London, 1970.
60. R.L. Fullman: *Trans. AIME*, 1953, vol. 197, pp. 447-52.
61. A.G. Franklin: *J. Iron Steel Inst.*, 1969, vol. 207, pp. 181-86.
62. J. Harkki and Y. Julin: *German-Finnish Symp.*, Report TKK-V-B 26, Helsinki University of Technology, Helsinki, 1984, pp. 39-51.
63. P. Ramdohr and H. Strunz: *Lehrbuch der Mineralogie*, Ferdinand Enke Verlag, Stuttgart, 1978.
64. E.T. Turkdogan: *Chemical Metallurgy of Iron and Steel*, The Iron and Steel Institute, London, 1973, pp. 153-70.
65. C. Wagner: *Z. Elektrochemie*, 1961, vol. 65, pp. 581-91.
66. C.C. Wang: Ph.D. Thesis, University of Wisconsin, Madison, WI, 1979, pp. 159-68.
67. W. Kurz and D.J. Fisher: *Fundamentals of Solidification*, 3rd ed., Trans Tech Publications, Switzerland, 1989.
68. S.O. Olsen: Bjølvefossen/Elkem, Ålvik, Norway, personal communication (1992).
69. O. Liesenberg, C. Podrzucki, and A. Bielat: *Giessereitechnik*, 1985, vol. 31, pp. 99-104.
70. R. Hummer: *Proc. 2nd Int. Symp. on the Metallurgy of Cast Iron*, Geneva, 1974, pp. 147-58.